Master's thesis

NTNU
Norwegian University of Science and Technology
Faculty of Natural Sciences
Department of Physics

Gyebi Alex Gyamfi

Magnetic Resonance Imaging (MRI) Quality Assurance Phantom and Protocol

Master's thesis in Master of Science in Physics (Biophysics and Medical Technology)
Supervisor: Pal Erik Goa
Co-supervisor: Kirsten Margrete Selnæs, Steven Inkoom
May 2023

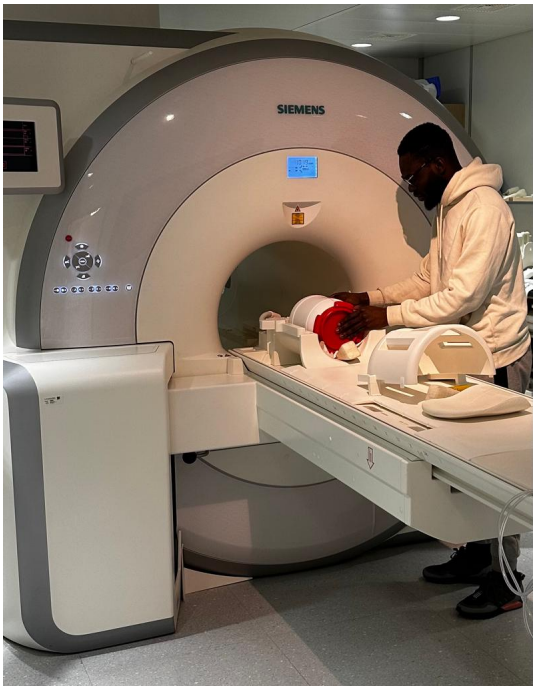

NTNU
Norwegian University of
Science and Technology

Gyebi Alex Gyamfi

Magnetic Resonance Imaging (MRI) Quality Assurance Phantom and Protocol

Master's thesis in Master of Science in Physics (Biophysics and Medical Technology)
Supervisor: Pal Erik Goa
Co-supervisor: Kirsten Margrete Selnæs, Steven Inkoom
May 2023

Norwegian University of Science and Technology
Faculty of Natural Sciences
Department of Physics

NTNU
Norwegian University of
Science and Technology

Abstract

Objective: To propose and design a low-cost, easy-to-manufacture, and highly efficient alternative quality control (QC) phantom and accompanying measurement protocols for MRI QCs.

Material and Methods: Widely available and affordable materials which are non-ferromagnetic were used in the phantom design. These materials include plastic and rubbers of legos, kitchen cutting boards, washer baskets, and plastic bottles. MRI image quality of 1.5 T and 3 T scanners were tested using the New Phantom and the ACR Phantom. A head coil was used to fix the phantom head position. A DICOM viewer software was used to analyze the images acquired.

Results: The maximum internal lengths and diameters were measured to be 148.70 mm and 189.83 on the 1.5 T scanner respectively with discrepancies of 0.7 mm and 0.17 mm for the geometric accuracy test using ACR Phantom. The New Phantom measured 254.10 mm and 190.76 mm with top errors of 0.9 mm and 0.76 mm in internal lengths and diameters. These measurements from the new phantom were within the acceptable limits of ± 3 mm. The new phantom also has the ability to check the same parameters as the ACR phantom, particularly in the low-contrast object detectability test where the new phantom was able to produce similar results as the ACR phantom. Additionally, the new phantom also showed excellent results for spatial resolution and had relatively fewer errors in ghosting measurements compared to the ACR phantom. Both phantoms also had acceptable measurements for image intensity uniformity, with the new phantom slightly exceeding the minimum acceptable limit. For image intensity uniformity, the minimum percent integral uniformity was 81.18 % and 86.28 for the New Phantom and the ACR Phantom which were within the acceptable limit of 80 %.

Conclusions: A new alternative phantom for MRI QC tests has been fabricated using widely available materials. Images acquired with this new phantom can be used to analyze geometric accuracy, high-contrast spatial resolution, ghosting, low-contrast object detectability, and image intensity uniformity tests. Using ACR and the New Phantoms, these tests showed acceptable image parameters.

Sammendrag

Mål: Foreslå og designe en billig, lett produsert, og svært effektiv alternativ kvalitetskontroll fantom og medfølgende måleprotokoll for MRI kvalitetskontroll.

Materiale og Metoder: Allment tilgjengelige og billige materialer som er ikke-ferromagnetiske ble brukt til fantom designet. Disse materialene inkludert plast og gummi fra lego, skjærebrett, skittentøyskurver og plastflasker. Bildekvalitet med 1.5 T og 3 T MRI skannere ble testet med både det nye Fantomet og ACR Fantomet. En hodespole ble brukt til å sikre korrekt hodeposisjon til fantomet. En DICOM-kompatiblet programvare ble brukt til å analysere de anskaffede bildene.

Resultat: Den maximale innvendige lengden og diameteren ble målt til henholdsvis 148.70 mm og 189.83 mm på 1.5 T MRI skanneren med respektive avvik på 0.7 mm og 0.17 mm for den geometriske nøyaktighetstesten ved bruk av ACR Fantom. Det nye Fantomet målte henholdsvis 254.10 mm og 190.76 mm med høyest unøyaktighet på 0.9 mm og 0.76 mm for innvendig lengde og diameter. Disse målingene for det nye fantomet var innenfor de aksepterbare grensene på $\pm$ 3 mm. Det nye fantomet har også evnen til å sjekke de samme parameterne som ACR fantomet, spesielt med tanke på synlighetstesten av lav-kontrast objekter hvor det nye fantomet gav lignende resultater som ACR fantomet. I tillegg viste det nye fantomet også utmerkede resultater for romlig oppløsning og hadde relativt færre feil i ghosting målinger sammenlignet med ACR fantomet. Begge fantomene viste aksepterbare målinger for uniformiteten av bildeintensiteten, hvor det nye fantomet såvidt overgikk den aksepterbare minimumsgrensen. For uniformiteten av bildeintensiteten var prosenten for minimum integral uniformitet på 81.18% for det nye fantomet og 86.28% for ACR fantomet, begge innenfor den aksepterbare grensen på 80%.

Konklusjon: Et nytt alternativ fantom for MRI kvalitetskontroll tester har blitt laget ved bruk av lett tilgjengelige materialer. Bilder tatt av dette nye fantomet kan brukes til å analysere geometrisk nøyaktighet, høy-kontrast romslig oppløsning, ghosting, synlighet av lav-kontrast objekter og bilde intensitet uniformitet tester. Ved bruk av ACR og det nye fantomet viste disse testene aksepterbare bildeparametere.

This work is dedicated to my late uncle Mr. Baffour Awuah Preprah for his immense support throughout my education.

Acknowledgment

Firstly, I want to express my deep appreciation to God for granting me wisdom, knowledge, understanding, and good health, as well as for providing all the necessary resources for this research. I give all the glory, honor, and praise to His Holy Name.
Next, I would like to acknowledge the PET/MRI Center at St. Olavs Hospital for their generous provision of resources that have been invaluable for this research.
Lastly, I would like to express my sincere gratitude to the NORPART Program for their financial support during my Master's degree studies.

Table of Contents

List of Figures

List of Tables

List of Abbreviations

MRI	Magnetic resonance Imaging
CT	Computed Tomography
QC	Quality Control
QA	Quality assurance
NMR	Nuclear magnetic resonance
SNR	Signal-to-noise ratio
MRS	Magnetic resonance spectroscopy
EEC	European Economic Communities
CNR	Contrast-to-noise ratio
ACR	American College of Radiology
ADNI	Alzheimer's Disease Neuroimaging Initiative
RF	Radiofrequency
B0	External Magnetic Field
T	Tesla
°K	Temperature in Kelvin
MHz:	Mega Hertz
B1	Electromagnetic field generated by the transmit coil
Tx	Transmit Coils
Rx	Receive coils
CP	Circularly Polarized
GA	Geometric Accuracy
AAPM	American Association of Physicists in Medicine
IPEM	Institute of Physics and Engineering in Medicine
$NiCl_2$	Nickel Chloride
$MnCl_2$	Manganese Chloride
PET	Positron emission Tomography
NaCl	Sodium Chloride
DICOM	Digital Imaging and Communications in Medicine
USB	Universal Serial Bus
LCD	low-contrast object detectability

CHAPTER ONE

1.0 INTRODUCTION AND BACKGROUND

Magnetic resonance imaging (MRI) is a more sophisticated and frequently used imaging modality in recent years due to advances in technology. MRI has been widely used in various fields, such as biology, engineering, and material science, due to recent technological advancements. Because of its ability to provide distinguishing soft tissue contrast that is typically superior to that of Computed Tomography (CT) and its high spatial resolution, MRI has completely transformed diagnostic imaging in medical science [1].

In diagnostic radiology, quality has been defined as the degree to which the correct process is performed in an appropriate manner, at the right time, and the right interpretation is relayed to the patient and referral physician accurately and quickly [2, 3]. Also, quality in MRI refers to a variety of factors such as the performance of scanners, operations of the clinic related to data-driven improvement, as well as efficient scanning and reporting utilizing the right performance metrics. The quality of MRI is dependent on two key components: quality control and quality assurance

1.1 Quality Assurance (QA)

Quality assurance (QA) is the process of preventing errors and defects in products. It encompasses the measures required to ensure that a service meets established standards. It additionally includes all of the systematic procedures within the quality structure that provide assurance that the imaging examination will meet the basic diagnostic quality requirements.

QA in MRI is a broad principle that encompasses all processes for the management processes developed by the MR imaging group, led by the MR supervising radiologist. The goal of QA is to make sure that [4]:

i. Each imaging procedure is essential and applicable to the clinical issue at hand.

ii. The images produced include vital details of information for problem resolution.

iii. The information recorded is properly interpreted and promptly made accessible to the physician of the patient.

iv. The risks, expenses, and discomfort to the patient, in accordance with the aforementioned objectives, are yielded during the examination.

1.2 Quality control (QC)

On the other hand, Quality Control (QC) determines whether the imaging product's quality meets expectations. An important part of quality assurance is QC. MRI QC refers to a set of basic tests that every MRI system must pass to ensure proper scanner performance, efficient clinical operations, accurate scanning, and reporting, as well as data-driven performance enhancement via appropriate performance metrics and the creation of high-quality diagnostic images [5, 6]. In summary, QC is a collection of unique technical processes that ensure the production of an acceptable product, in this instance, excellent diagnostic images [4]. The following steps are involved:

i. One way to ensure that newly installed equipment or equipment that has undergone major repairs is working properly is by performing acceptance testing to detect any defects.
ii. QCs are used to establish baseline performance of the equipment mostly during acceptance testing and commissioning.
iii. Changes in equipment performance are detected and diagnosed before they appear in images.

iv. Check to see if the causes of equipment performance degradation have been addressed.

In the early 1980s, signal quality and signal-to-noise ratio (SNR) measurements were used to assess the stability of MRI scanners [6]. A specially developed MRI phantom was launched in the late 1980s for the QA of nuclear magnetic resonance (NMR) and magnetic resonance spectroscopy (MRS) scanners. Magnetization relaxation times were then measured to quantitatively assess various physical characteristics of signal quality as a means to evaluate scanner performance. However, these investigations were limited in providing comprehensive information about image quality [6].

As a result, the European Economic Communities (EEC) implemented quality assurance procedures and methods based on Eurospin, a collection of test objects that are uniquely designed [6]. The European Concerted Action "Tissue Characterization by MRS and MRI" (COMAC-BME) has made significant contributions to (MRI) quality control. Image quality measurements such as geometric distortion, spatial resolution, signal uniformity, SNR, contrast-to-noise ratio (CNR), and slice thickness were included in these QA protocols [6].

The entire development history was described, as well as guidance for the measurement types that could be made with such test objects, and examples of the results are outlined in Eurospin test objects [6]. The Eurospin encompasses a range of phantoms for MR tests for various applications and objectives, which could be used to check the most important performance aspects of an MRI scanner. However, these systems pose challenges in clinical field use due to their high cost-effectiveness and complexity [6].

Several studies have credited the use of new protocols and phantom designs for improving the image quality of clinical MRI scanners [7-10].

The American College of Radiology (ACR) has recently introduced an optional MRI accreditation program. The program is structured similarly to the ACR Mammography Accreditation Program, which has implemented mammography quality assurance (QA) and quality control (QC) techniques and standards. [4]. The QA and QC protocols for MRI machine quality control are based on the guidelines provided by the American College of Radiology. Currently, for the purposes of quality control, ACR phantoms are used. Other previous efforts to create standard phantoms that have been successful include the Pro MRI Kit Phantom and the Alzheimer's Disease Neuroimaging Initiative (ADNI) MRI Phantom [11]. However, these commercially available phantoms can be expensive and may not be widely accessible in developing countries like Ghana.

As a result, there is growing interest in low-cost and simple-to-make alternative QC phantoms. The goal of this study, therefore, is to explore such alternatives in pursuit of:

1) Reviewing the hardware components of MRI, including magnets, radio frequency coils, gradients, and the computer system, and the measurement techniques required to assess their performance.
2) Reviewing the existing quality assurance phantoms (such as the ACR phantom) and protocols.

3) Proposing a low-cost, easy-to-manufacture, and highly efficient alternative phantom and accompanying measurement protocols.

4) Implementing and comparing the results acquired with the new phantom with the existing (ACR) phantom on a set of clinical MRI systems.

CHAPTER TWO

2.0 LITERATURE REVIEW

2.1 MRI HARD COMPONENTS

2.1.1 Review of MRI hardware components

To generate magnetic resonance images, multiple procedures must be completed, including image acquisition and image formation. Different system components, including hardware or equipment and software programs (pulse sequences and image formation programs), are needed to complete these processes. These processes include alignment of the nuclei, excitation of nuclei using radio frequency, spatial encoding, and formation of the image. In contrast, the main hardware components needed to complete such processes include Magnet (for alignment of nuclear) with patient table, a radiofrequency (RF) source (that is RF transmit RF receive) for nuclei excitation, a gradient system for spatial encoding, and computer system (for image formation and other user interface) with image processor [12]. This system is demonstrated below in Figure 2.3.

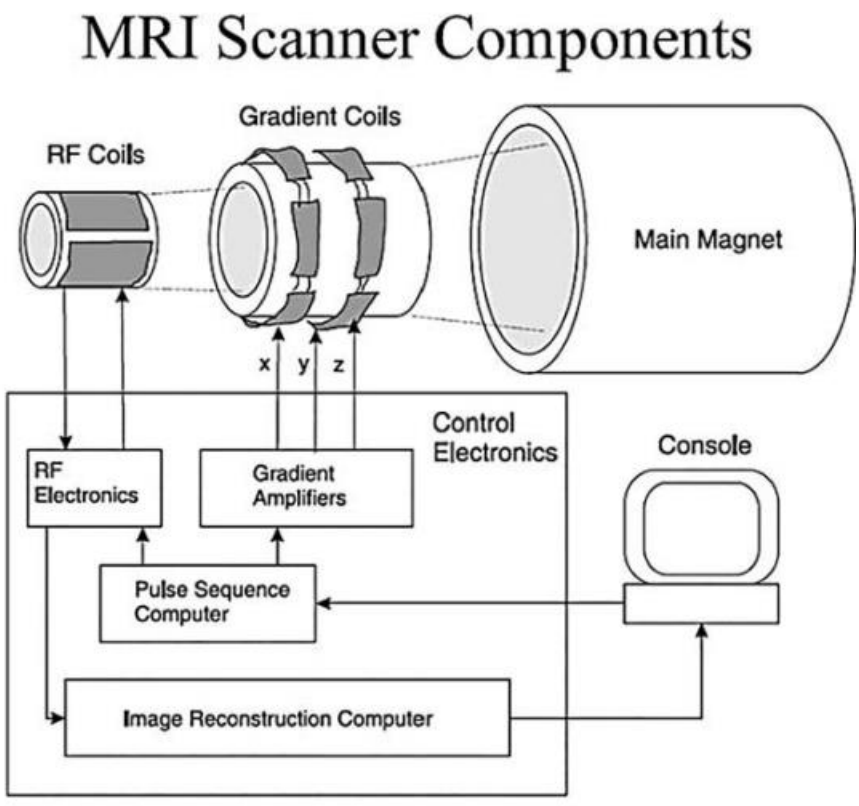

Figure 2.3. A schematic diagram illustrating the basic component of an MR system [13] granted access.

2.1.2 MR Magnet

The magnet is the basic component of the MRI system. The MR magnet is responsible for aligning the nuclei to the external magnetic field. Depending on the energy of the nuclei, they are aligned either parallel or antiparallel with the external magnetic field, B0. Low-energy nuclei lie parallel with B0 while high-energy nuclei lie antiparallel with

B0. The stronger the magnet the more nuclei spin aligns parallel and the more spins are in excess, the greater the signal and thus the better the image quality. All magnet field strengths are measured in tesla or gauss units where 1 tesla is equivalent to 10,000 Gauss [12]. Most clinical MR systems range in strength from 0.2 Tesla (T) to 4 Tesla (T). There are also imaging systems used in clinical settings that have ultra-low magnetic fields (0.01 T) and ultra-high magnetic fields (10 T), but they are uncommon. The parameters of the MR magnet are categorized into low, medium, and high fields. Low-field magnets are magnets with external field strength between 0.2 T and 0.4 T. Medium fields are usually in the range of 0.5 T to 1.5T with high fields ranging from 1.5 T and 3 T while ultrahigh field systems have field strength greater than 3 T. The magnets that are used for MR images can also be characterized as permanent, electromagnets (solenoid), resistive, superconducting, or hybrid magnets.

2.1.2.1 Permanent magnets

These magnets are made of materials that retain their magnetic properties for extremely long periods of time. These are known as ferromagnetic substances. Iron, nickel, and cobalt are a few examples. The most frequently used permanent magnet material is alnico, an alloy of aluminum, nickel, and cobalt. Permanent magnets have minimal maintenance costs but must be kept away from a ferromagnetic material and have their mass concentrated over a small area [12,14].

2.1.2 .2 Electromagnets (solenoid)

Electromagnets are another type of magnet in which the magnetic field is generated by the flow of electrical current through wire coils. Once there is a flow of current through the magnet windings, a magnetic field is generated according to Faraday's law of electromagnetic induction. Conventional electromagnets are constructed of copper wire wound in a variety of loop shapes. They may also be designed as solenoidal or open-type. A constant current source is provided by a power supply. Because copper wire can only carry a limited amount of current, copper wire-based electromagnets are low-field systems. They are also susceptible to changes in room temperature. A strong magnet can be formed by connecting two current-carrying wires. Rather than using multiple parallel wires, a single wire can be wrapped around to create multiple loops. The wire loops form a coil and act like parallel straight wires. A solenoid electromagnet is a spring-like electromagnet [12].

2.1.2.3 Resistive magnets

At room temperature, an electromagnet obeys Ohm's law and is referred to as a resistive magnet. The magnetic field strength of a resistive magnet is determined by the current flowing through its wire coils. The magnetic field strength of a resistive magnet is determined by the flow of current through its wire coils. The highest field strength is less than 0.2 T or 0.3 T, and the magnetic field can be instantly switched off with the flip of a switch. It is lighter in weight than permanent magnets, but it has a high cost of operation due to the large amounts of power essential to maintain the magnetic field [12]

2.1.2.4 Superconducting magnets

To make a superconductive MRI magnet, a solenoid-shaped coil that is made from alloys such as niobium/titanium or niobium/tin surrounded by copper is used. When cooled to about a temperature of 10 kelvin, these alloys have zero resistance to electrical current. The coil is cooled down by liquid helium to this temperature [12]. In order to avoid helium loss, a helium 'liquefier' is used. The power supply is connected on either side of a short-heated segment of the coil, and the current flowing through the coil gradually increases over several hours to achieve the required magnetic field. To generate a field strength of say 1.5 T, a high amount of current between 300-700 A is required. The use of copper acts as an insulator, preventing the alloy coil from being destroyed in the event of a quench, which can result in superconductivity loss and potentially fatal consequences [14].
In a cryostat, the main magnet windings are immersed in liquid helium (4°K). The cryostat is a multi-part structure with main magnet windings, liquid helium channels, insulating and vacuum layers, superconducting shim coils, and active shielding coils [15]

2.1.3 Gradient Coils

Gradients are loops of wire or thin conductive sheets wrapped around a cylindrical shell that sits just inside the bore of a magnetic resonance imaging (MRI) scanner. Once current is passed through these coils, a secondary magnetic field is formed. The gradient field causes changes in the field strength causing a change in the resonance frequency of the nuclei. A gradient refers to a slope, in this instance a very linear slope in magnetic field strength through the imaging volume in a particular direction. There are three sets of gradient coils for an MR system which are the x, y, and z- gradients. The MR gradients are needed for spatial localization of slice, spatial encoding of signal, and contrast encoding (for example, diffusion and phase contrast) [16]. The strength and linearity of the gradient coils are critical parameters that affect the quality of the MRI images. The strength of the gradients determines the resolution of the images, while the linearity of the gradients determines the accuracy of the spatial encoding. If the gradient coils are not sufficiently strong, the image resolution will be poor, and if the gradient coils are not linear, the spatial location of the nuclear spins will not be accurately encoded, leading to geometric distortions in the images. It is, therefore, important to evaluate the performance of the gradient coils using various quality assurance measurements, such as image uniformity, signal-to-noise ratio, spatial resolution, and geometric distortion or geometric accuracy. To ensure that the gradient coils are performing optimally, regular quality control tests should be performed on the MRI system. These tests may include checking the gradient coil's strength and linearity using specialized test objects, measuring the image uniformity and signal-to-noise ratio, and evaluating the spatial resolution and geometric distortion of the images. Errors in the gradient coils can have a significant impact on the QA results. For example, it may not be possible to generate images with a high spatial resolution for weaker gradient coils. In a likewise manner, if the gradient coils are nonlinear, there would be distortions or inaccuracies in the images which makes it difficult for accurate diagnosis [12, 16]

2.1.4 Radiofrequency (RF) Coils

RF coils are a critical piece of MRI hardware. They have a direct impact on MRI spatial and temporal resolution, sensitivity, and uniformity. The RF coils are used for transmission of electromagnetic RF pulse for excitation of the nuclei in the patient/sample. Another purpose is also to receive signals from the nuclei [13]. The small magnetic field generated by the RF pulse produced from the radiofrequency transmit coil rotates the net magnetization from its original alignment to the main field. The greater the strength of the radiofrequency pulse, the greater the flip of the magnetization. The angle of tilting is referred to as the flip angle [13].
The electromagnetic field B1 generated by the transmit coils is perpendicular to the main magnetic field B0 and oscillates at the resonance frequency, which is referred to as the Larmor Frequency. The Larmor frequency is determined by the nucleus type and the strength of the main magnetic field. The range of frequency of radio waves (MHz) corresponds to this precession frequency. In magnetic resonance imaging, it is common to use a body coil located in the bore of the scanner for transmitting signals into the body. This body coil is designed to generate a strong and uniform magnetic field to excite the protons in the body tissue. After the protons are excited, they emit radiofrequency signals that are then detected by various receive-only coils that are placed around the body part of interest. These receive-only coils are designed to be sensitive to the radiofrequency signals emitted by the excited protons and convert them into electrical signals that can be processed to create images. By using different receive-only coils, the sensitivity and resolution of the imaging can be optimized for different body parts and applications. There are several types of receive-only coils, including surface coils, phased array coils, and volume coils. For the purpose of this project, the body coil in the MRI scanner was used for transmission while a receive-only head coil was used for signal detection [12, 13]. The size and shape of RF coils vary depending on the area of the body being imaged and the imaging protocol used. The size and shape of the RF coil can influence the magnetic field's homogeneity and the penetration of the RF pulses into the tissue. As a result, choosing the right RF coil is critical for obtaining high-quality images. Various QC measurements including image uniformity, RF coil sensitivity measurements, signal-to-noise ratio, and contrast-to-noise ratio tests can be used to assess the efficiency of the RF coils. These measurements assess the RF coil's ability to transmit and receive RF signals effectively, and any deviations from optimal functioning can impact image quality. For example, if the RF coil is not transmitting or receiving RF signals correctly, it can result in poor image resolution, contrast, or signal-to-noise ratio [4,5,10,12].

2.1.4.1 Types of RF coils and their application

RF coils can be differentiated for example, by the homogeneity of their B1 field or, from a usage standpoint, into Surface Coils, Array Coils, and Volume Coils.
The Volume coils are cylindrically designed coils that are mainly used to excite nuclei only but can also be used as transmit and receive coils. By their technology, they are circularly polarized with a birdcage design. It is designed in such a way that it produces an RF excitation field, B1 which is uniform throughout the whole volume [16, 17, 18, 19]. Surface coils are specialized coils of varying sizes that are used to receive signals from very localized regions. Surface coils have a higher signal-to-noise ratio when they are compared to volume coils. They are made up of a partial loop of wire with dimensions corresponding to the region of interest and inductance in resonance with capacitance at the Larmor frequency. They can be combined together to form an array that can be used to enhance the signal-to-noise ratio over a large region of interest. The use of array coils requires careful management to prevent crosstalk between the coil elements, which can reduce the efficiency of signal-to-noise [13]. Figure 2.4 shows different types of configurations of coil arrays.

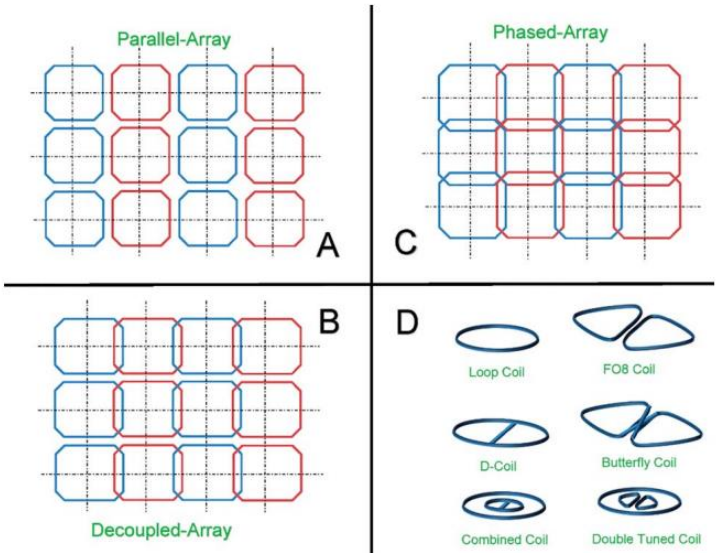

Figure 2.4. Different types of array coil combinations: (A) parallel array, (B) decoupled array, (C) phased array, (D) representation [13] copyright access granted

2.1.4.2 Transmit Coils (Tx)

To excite the spins in the sample, one uses the RF coil transmitter. This is accomplished by sending to the sample of interest a well-defined RF pulse. Ultimately, the goal of the RF transmit coil is to produce a uniform B1 1 -field. Another goal is to also reduce the time required to shift the net magnetization from its original state. [12, 13]

2.1.4.3 Receive Coils (Rx)

The receive coils are used in receiving the signals from the nuclei. For very good reception, receiver coils need to have a high signal to noise. Smaller coils are better than larger coils and produce higher SNR but they have smaller sensitivity areas. For better SNR, there should be more coil elements [12, 17].

2.1.4.4 Coil technology

RF coils could also be classified by means of their technology and how they are manufactured. These technologies of coils include but are not limited to linear coils, Quadrature coils/Circularly Polarized (CP coil), Phased array coils, Transmit only coils, Receive only coils, Transmit and receive coils, Surface coils, and Volume coils. Linear coils are just a loop of wire that gives a B1 field along only one axis. It is a simple coil technology design with a loop

perpendicular to the field B0. For reception as a surface coil, it provides high SNR when scanning structures near the patient's surface and the coil. Circularly polarized coils are coils that are configured with multiple coil elements that are phase shifted to each other and produce a B1 field that rotates with the net magnetization vector. CPs have very efficient energy transfer and a more homogeneous B1 field than linear coils. CP coils improve reception SNR by √2 when compared to linear coils, because we sample both the noise and the signal twice. The next coil is the phased array coil which receives signals from several coil elements (>4 and not unusual with 32 channels on clinical scanners) at the same time. They need several receiver channels (one for each coil element) with each element having the same SNR as a surface coil. Phased array coil uses parallel imaging techniques. The body coils are cylindrical in design and are mainly used for the excitation of nuclei only but can also be used as transmit and receive coils and are usually circularly polarized and birdcage designs.
Coils that are normally used in anatomical imaging around the head are the head coils. They are small cylindrical coils which usually are volume coils with CP design. A phased array is the most common design for receiving coils [16, 18].

2.1.5 Computer Systems

The computer system is one of the important components of an MRI system. The various computer systems in an MRI scanner execute a number of operations. Data collection and processing, image display, radio frequency, and gradient pulses are primarily controlled by these computer systems. The computer samples the incoming signal at discrete time intervals and processes the data into recognizable images. The computer system also has a console that is used to display images and some text information.

2.2 Review of Existing Phantoms

2.2.1 The ACR Phantom versus the New Phantom

The ACR MRI phantom is a short, cylindrically hollow phantom made of acrylic plastic which closes at the ends of the phantom. The dimensions of the phantom are 190 mm in diameter and 148 mm in length on the inside. A nickel chloride and sodium chloride solution with concentrations of 10mM and 75mM respectively are used to fill the phantom. Furthermore, the phantom's exterior is etched with the words ``NOSE " and" CHIN " (figure 2.0) to assist in positioning the phantom to scan, as though the phantom were a human head. In the next section, the instructions for using the large MRI phantom are clearly outlined [20].

Figure 2.0. Illustration of ACR-MRI-Phantom [21] open access

2.2.2 Guidelines for Phantom Test Measurements

2.2.2.1 Geometric Accuracy (GA)

The accuracy with which an image depicts the subject's length is assessed using the geometric accuracy test. By using easily identifiable locations on the image acquired from the phantom, the lengths are measured and the results are compared with the true lengths of the phantom [20]. Within the ACR phantom, there are seven sets of known length measurements taken with the software's on-screen length measuring tool. Additionally, the display window and level must be properly configured to avoid affecting the length measurements, as they can change the apparent location of the phantom's edges which could introduce some errors in the accuracy of the length measurements. To overcome this limitation, image analysis should be performed by setting the display window width and the window level to the mean signal value and half the mean signal value respectively at regions in the image where there is water only [20]. In the newly developed phantom, however, there were eight sets of known length measurements with a diameter measurement in the sagittal localizer which was the additional length included. This further helps to verify the diameter dimension on the inside which could be compared to the diameters of the axial slices. A failure in the geometric accuracy test would result in image dimensions differing significantly from the true dimensions, indicating an issue with the scanner's proper operation. Image distortion caused by improperly calibrated magnetic gradients can also result in scanner failure, leading to changes in the lengths of the associated dimensions (x, y, or z) in the images compared to their real values [6].
Acquiring images with extremely low bandwidths is a common practice to improve the signal-to-noise ratio (SNR), but it can also result in image distortion due to the normal heterogeneity of the main magnet. In addition to the aforementioned causes, abnormally high magnet heterogeneities may also result in a test failure [20].

2.2.2.1.1 Analysis of the Measurements

To analyze data for GA, the measured lengths are compared to the true internal dimensions of the phantoms. The sagittal length of the ACR phantom measures 148mm while the axial diameter measures 190mm and that of the New phantom measures 190 mm and 255 mm in diameter and length respectively.

2.2.2.2 High-Contrast Spatial Resolution

In the high-contrast spatial resolution test, small objects are resolved by the scanner at a high enough contrast-noise ratio to the extent that it would not limit the capacity of the scanner to resolve details. However, the test is not without potential failures. If the scanner fails this test, it means it does not resolve small details compared to a well-functioning scanner for a given field of view and acquisition matrix size. It's worth noting that clinical parameters are usually tweaked to optimize for high contrast resolution, and if there is a failure in a site for resolution test in either of the series, then the test must be done on the site series [20].

In this test, a visual evaluation is performed on the resolution insert. The insert in the ACR phantom is a plastic block with drilled holes of varying sizes which is filled with the phantom solution. The resolution insert is made up of three pairs of holes which are not-quite-square arrays of holes. It is made up of a top left array of holes and a bottom right array of holes, where right and left refer to the right and left sides of the viewer. The top left array of holes and the bottom right arrays share a single hole at the intersection. To evaluate resolution in the right-left direction the top left array is used, while the bottom right array evaluates resolution in the top-bottom direction.

The Top left array is made up of four different holes and four rows where the distance between holes on a row is two times that of the diameter of the hole. Additionally, the distance between center-to-center rows is two times the diameter of the hole, with the staggered arrangement ensuring that at least a single row's hole perfectly aligns with the display matrix, which allows each to be focused within a pixel. There is an exhibition of partial volume effects which would result in blurred and irregularly shaped signal spots for holes that are misaligned with the display matrix.

Nevertheless, the inserts in the new phantom are plastic combs with varying line spacing and holes of different diameters drilled on the central part of the double-edged comb. The first comb has two different lines spacing on the left and right sides while the second comb has the same line spacing on both the upper and lower parts. The spaces between the lines of the comb together with the holes which are filled with the solution of the phantom are used as objects of high contrast for the high-contrast object detectability tests in the new phantom. The new phantom can resolve objects as small as 0.5 mm which makes it unique compared to the ACR which has the smallest resolvable object of 0.8 mm. This is accomplished by visually inspecting the 0.5 mm upper and lower line spacing on the double-edged com.

2.2.2.3 Slice Thickness Accuracy

The slice thickness test verifies that the scanner produces slices with the desired thicknesses and measures the precision of achieving a specific thickness of the slice. To assess this test, the measured slice thickness is compared with the prescribed thickness of the slice. If the scanner fails the test, then it means that it is giving slices with significantly different thicknesses from the truly prescribed thickness. Failure of this can have implications on image contrast and signal-to-noise ratio, potentially leading to incorrect results [6].
In the slice thickness test, two lengths of axial series signal ramps are measured for slices showing the thickness insertion of the ACR phantom. These ramps are a component of a structure known as the slice thickness insert. The two ramps are crossed, one with a negative slope and the other with an opposite slope in relation to the plane of the slice with the insert. To produce these ramps, a 1mm wide slot in a block of plastic is cut and filled with a solution that was used to fill the entire phantom. The slope of the signal ramps in relation to the plane of slice 1 is 10 to 1, corresponding to an angle of about 5.71°. As a result, signal ramps with a length 10 times the thickness of the slice will appear in the image of slice 1.
One ramp will appear longer than the other if the phantom tilts to the right or left. The existence of crossed ramps corrects the error caused by the right-left tilt, and the formula for slice thickness stated in the following paragraph takes this into account [20]. The slice thickness insert could not be produced for the new phantom. Production required special equipment which is not widely available. This limits the phantom's ability to perform accuracy of slice thickness. This could however be included in future upgrades of the phantom.

2.2.2.3.1 Analysis of the Measurements

To compute the slice thickness, one can use the following formula:

$$Slice\ thickness\ = 0.2 \times (top \times bottom)/(to + bottom) \quad (1)$$

where top and bottom are defined as the lengths that are measured signal ramps top and bottom.

2.2.2.4 Slice Position Accuracy

The slice position accuracy test evaluates the precision with which slices can be prescribed at specific locations using the localizer image as a reference position. If this test fails, then it implies that the true positions of obtained slices deviate significantly from their required positions, which is out of the ordinary for a properly operating scanner. To assess for accurate location of the slices, the prescribed and actual slice positions for slice 1 and slice 11 discrepancies are measured for both ACR T1 and ACR T2 images. The crossed wedges appear as a pair of adjacent, dark, vertical bars at the top of the phantom on slices 1 and 11. Slices 1 and 11 are shown in Figure 2.1 which indicates crossed wedges vertical bars. The wedges are seen as dark bars of the same length if the slice is perfectly aligned with the vertex of the crossed wedges for each of slices 1 and 11[20].

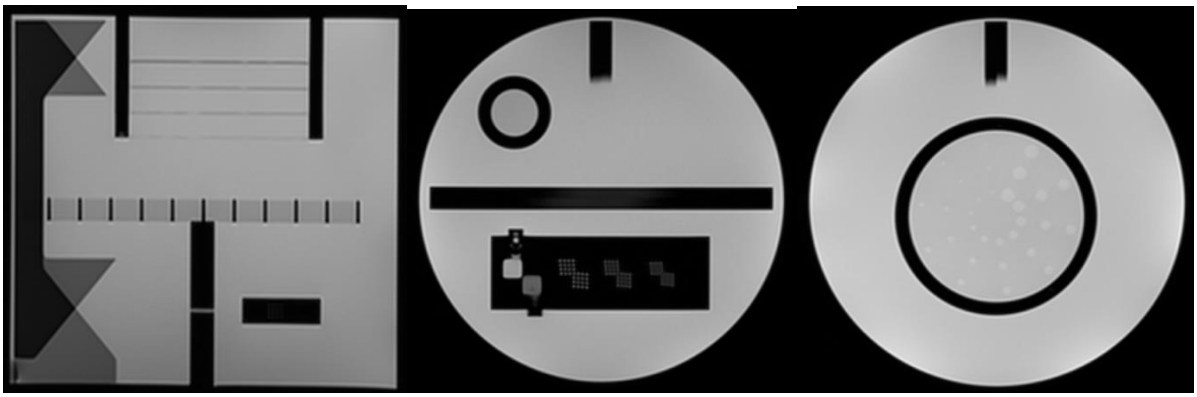

a b c

Figure 2.1 An image of a) sagittal image b) Slice 1 showing exactly aligned vertex of the crossed wedge c) Slice 11 showing mispositioned crossed wedges. All images were acquired from the 3 T scanner at St Olavs Hospital

2.2.2.5 Image Intensity Uniformity

In the region of the phantom that contains water only, the uniformity of image intensity is assessed using the image intensity uniformity test for both ACR and the new phantom. This area is located near the center of the imaged volume and the head coil for the ACR phantom. However, this region in the new phantom is located on the upper part of the phantom just before the thick slit inserts which lie on the walls of the phantom. In clinical settings, head coils have a fairly uniform spatial sensitivity near the middle of the coil when loaded in a typical manner for a human head. The head coil is able to cover this region where uniformity is measured for the new phantom. If the image intensity uniformity test fails, it means that the scanner has significantly more variation in image intensity than a properly functioning system. Phantom mispositioning, ghosting, and failure of the head coils are all potential causes of failure in the uniformity test. Furthermore, the phantom's instability, such as motion and vibration, may create a ghosting signal that affects the uniformity of the image intensity. This effect is observed for the new phantom when it is not allowed to sit for some time for the solution to settle before scanning.
In addition, a lack of image intensity uniformity is an indication that there is a flaw in the scanner, which is frequently caused by a faulty head coil or an error in the radio-frequency components. The percent integral uniformity (PIU) is calculated by using the signal values of low and high regions. PIU is computed using the following formula:

$$PIU = 100 \times (1 - (high - low)/(high + low)) \quad (2)$$

where; high and low are defined as measured high-signal and low-signal values in this formula [20].

2.2.2.6 Percent-Signal Ghosting

The percent-signal ghosting test determines the amount of ghosting in the images. Ghosting is an artifact that occurs when an indistinct copy of the imaged object shows up on the image, displaced from its true position. During this test, the level of the ghost signal is determined and then presented as a percentage of the signal level in the actual image. They are most visible in regions of the image with no signal. They can, however, overlay the main parts of the image and alter the intensities of the true image. The ghosting mostly occurs in the phase's encoding direction for the spin echo sequence which is used during the scan. Therefore, four ROIs are placed on the background along the four edges of the FOV so that two of the ROIs will be in the phase encoding direction when using the ACR phantom. This is easily done with the new phantom as well. The same region which was used for the uniformity test for the new phantom is used for the ghosting test but at this time keeping track of the mean pixel value.
If the test fails, it means that there is a much higher level of signal ghosting compared to there is signal ghosting in a correctly operating scanner. The ghosting value is calculated the following formula:

$$Ghosting\ Ratio = |((top + bottom) - (left + right))/(2 \times (large\ ROI))| \quad (3)$$

where; top, bottom, left, right, and large ROI are defined as the mean pixel values for the ROIs and the vertical bars on each side of the equation indicates that only the magnitude of the enclosed value is taken [20].

2.2.2.7 Low-contrast object detectability

For a properly functioning MR scanner, objects of low contrast should be clearly distinct from each other. A low-contrast object detectability test is required to evaluate the degree to which objects of low contrast are distinguished in the image. The low-contrast objects in the phantom have different sizes and contrast. The contrast-to-noise ratio (CNR) of the image is the primary factor that determines the ability to detect objects of low contrast. Scanners with different field strengths perform differently in terms of CNR, and clinical scan parameters are usually adjusted to account for these differences [20].
If this test fails, it means that the scanner's images contain far fewer low-contrast objects than most correctly functioning clinical scanners [20]. In the ACR phantom, four sections of the phantom contain low-contrast objects. The low-contrast objects appear as rows of small disks in each slice, radiating from the center of a circle like spokes on a wheel. Each spoke is made up of three disks, and each slice contains ten spokes.
The contrast on all disks on a given slice is the same. The diameter of all the disks in a given spoke is the same. Starting at 12 o'clock and working clockwise, the disk diameter gradually decreases from 7.0 mm at the first spoke to 1.5 mm at the tenth spoke. On the contrary, the low-contrast object for the new phantom is a round disk of polypropylene plastic. There are two disks for this phantom which appear on four different slices with each slice having seventy-five spokes and a total of three-hundred spokes on all four slices. The diameter of the spokes differs for each half circumference of the spoke and decreases towards the center of the slice. The hole diameter ranges from 1 cm from the lower half of the circle to 7mm in the middle and 5 mm from the upper part of the disk to 3 mm towards the middle. The higher number of spokes increases the accuracy of the phantom for low-contrast tests.

2.3.0 Review of Pro MRI Phantom Kit

The Pro-MRI Phantom is an MRI Phantom that allows for the comprehensive evaluation of critical imaging parameters. For calibration purposes, the phantom can be used to measure absolute values. It is also designed to be time-efficient for daily quality assurance [22]. The phantom is designed by Standard Imaging. The accompanying measurement supported by the phantom kit includes the following:

1. Geometric Distortion
2. Spatial Resolution
3. Slice thickness and position accuracy
4. T1 and T2 values
5. Interslice Gap check
6. Estimation of Image Bandwidth
7. Low Contrast Detectability test
8. Image Uniformity
9. Signal-to-Noise Ratio (SNR)
10. Physical and Electronic Slice Offset
11. Landmark positions

It is a versatile phantom for ACR, AAPM, and IPEM compliance testing (220 or 180mm in diameter). It is, however, very expensive, even when compared to the ACR phantom [22, 23]

2.3.1 Standard Phantom for MRI

In a recent article published by Stupic et.al, a standard phantom for MRI system was designed and built by the International Society of Magnetic Resonance in Medicine ad hoc committee on Standards for Quantitative MR to evaluate scanner performance, stability, comparability, and quantitative relaxation time imaging accuracy. The phantom is a spherical structure that is 200 mm in diameter. It contains a 57-element fiducial array, two relaxation time arrays, a proton density/SNR array, and resolution and slice-profile inserts. This is clearly illustrated in Figure 2.2. It can be used to characterize the performance of the scanner, monitoring of the scanner over time, and

comparing scanners. However, there are safety concerns because the phantom was filled with a solution of $NiCl_2$. Another significant worry is the phantom's cost. Standard imaging protocols for assessing geometric distortion, image uniformity, T1 and T2 mapping, image resolution, slice profile, and SNR were presented [24]. The desired measurements included were:

1. Radio frequency (RF) field, B1, non-uniformity
2. Static main magnetic field, B0, non-uniformity
3. Geometric linearity
4. Gradient amplitude
5. Slice position and profile
6. Image uniformity
7. Resolution (high-contrast detectability)
8. Signal-to-noise ratio (SNR) (low-contrast detectability)
9. T1 and T2 proton spin relaxation times, as well as proton density, are measured with accuracy and precision.
10. System constancy

Although the two phantoms mentioned earlier have been useful for quantitative purposes, they may not be suitable for the development of the new phantom, as the quantitative aspects may not be necessary for the intended use in this project. Consequently, all measurements of different parameters will then be compared with those obtained from the ACR phantom.

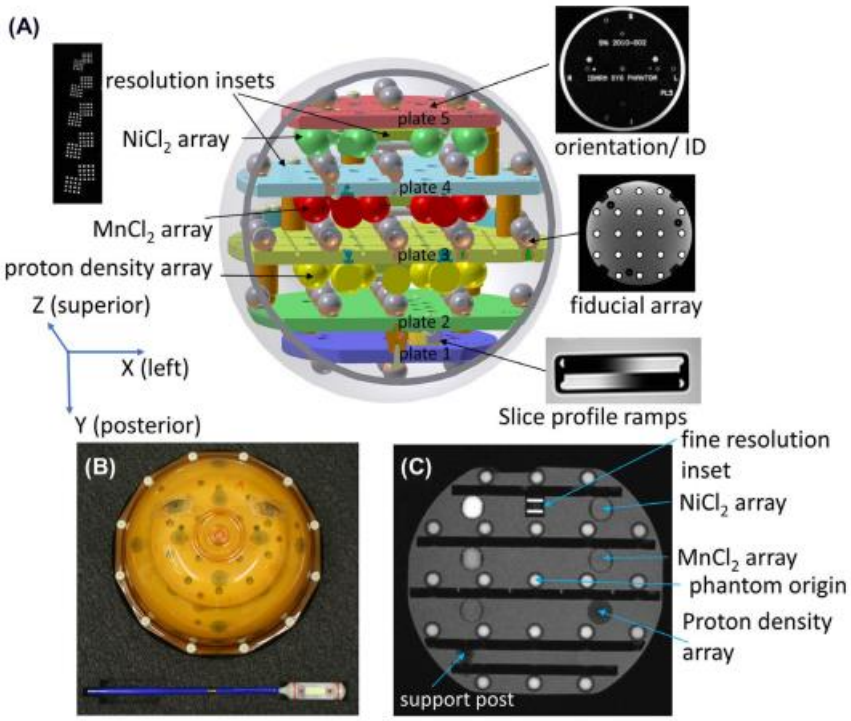

Figure 2.2 Fiducial arrays (gray/brown), $NiCl_2$ arrays (green), $MnCl_2$MnCl2 arrays (red), proton density arrays (yellow), and resolution and slice profile insets are shown in this system phantom schematic. The serial number and phantom type are visible MR engravings on Plate 5. All plates have orientational marks, and plate 3 has a grid for manually estimating geometric distortion. B, The phantom's top view with eye decals. The MR parameter arrays, fiducial elements, phantom origin, and resolution insert are shown in C, Y-Z sagittal slice [24], open access.

CHAPTER THREE

3.0 METHODOLOGY

3.1 Study Design and Center

The study was conducted at St. Olavs University Hospital, Trondheim-Norway. The measurements were using quality assurance and control procedures designed by the hospital and guidelines from the ACR large and Medium Phantom measurements. The study was conducted on two clinical MR scanners which are in clinical operation, the MAGNETOM Avanto fit 1.5T (Siemens Healthineers, Erlangen, Germany) and the Biograph mMR (3T PET/MRI system) (Siemens Healthineers, Erlangen, Germany).

3.2. The Phantom Design

For the purpose of the phantom development, it was expedient to use a container that is non-magnetic. The phantom was therefore constructed from materials of acrylate plastic, ethylene plastic, and glass without any ferromagnetic materials.
A plastic bottle with a screw lid closure was used to harbor all the phantom inserts and the solution was used to fill the phantom. The unit plastic bottle has a wide mouth of 136 mm diameter opening which allows easy insertion. The internal dimensions of the bottle are 190 mm in diameter and 255 mm in sagittal length. This bottle is made up of plastic and has a leak-tight lid to prevent the solution from spilling out [25].
One readily available material which could potentially mimic objects of low contrast was the kitchen plastic cutting board. The Farberware cutting board consists of polypropylene plastic and is thus non-magnetic. Polypropylene plastic was an ideal material for designing the low-contrast disc due to its water resistance [26]. The low contrast object detectability disc was the first portion of the phantom that was therefore designed. To do this, a 1.5 cm thick round disc with a diameter of 13.6 cm was cut from the kitchen chopping board. Holes of different diameters were perforated through the disc to mimic objects of low contrast. The diameters of the holes were 10mm, 9mm, 8mm, 5mm,4mm, and 5mm towards the center of the disc, as shown in Figure 3.1. To ensure that hole separation and hole diameters were dimensionally correct, a cross mark through the midline of the round disk was made.
For the geometric accuracy test, square grids of the internal area $22 \times 22\ mm^2$ were cut from a glasswasher basket. This washer basket is made from a special polypropylene that will resist water through it [27]. It is also non-magnetic and thus ideal for a creative phantom insert. The dimensions for the square grids are equal and thus it makes the square grids an ideal replacement for that of the ACR for the geometric accuracy test. The square grids of the inside of the basket were cut which was used as part of the phantom insert for the geometric accuracy test. The square grids allow for axial diameter measurement in four directions for the GA test. One can measure top-to-bottom, left-to-right, and two diagonals. The grids were held strongly in the middle of the phantom by two transparent plastic slits of wedges that lie opposite to each other on the sides of the internal walls of the bottle.
Lego bricks of different shapes and sizes were used to mount the round disc inside the midline of the bottom part of the bottle together. The Lego bricks are plastic materials made of Acrylonitrile Butadiene Styrene (ABS) [28, 29]. To keep the inserts in position, adhesive glue was used to stick them together at the bottom edge of the bottle.
A 7 mm thickness of chopping board was cut and used to keep grids in position rising from the bottom of the bottle through the sagittal plane. To access high-contrast spatial resolution for the bottle phantom, a double-edge comb with 0.5mm line spacing on each side was used. Holes of diameter 1.5mm and 1.0mm were drilled through the center of the double-edge comb. Another comb of line spaces 0.8mm, 1.2mm, and thicknesses 0.9mm and 1.2mm were also inserted to double-check the spatial resolution test. The bottle was then filled with 75 mM NaCl solution to the fullest for biological conductivity. They were then closed and tightened using the screw lid closure. A sagittal and axial line was drawn through the middle of the phantom to be used for scanning setup and positioning. The phantom's geometry allowed it to be placed on the coil housing with a z-axis orientation and location relative to the RF coils. The figures below show images of the materials used for the phantom design.

a b

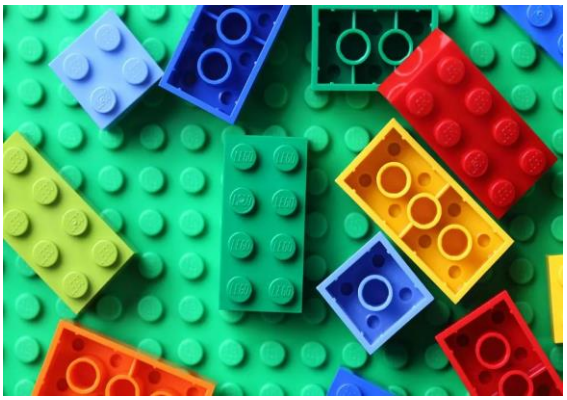

c d

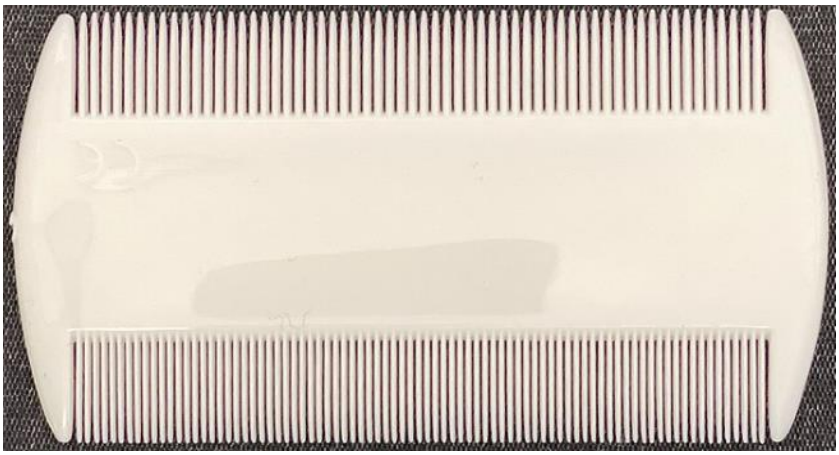

e

Figure 3.0 Illustration of materials used for phantom insert design. (a) Plastic bottle with screw lid closure (b) Lego bricks (c) washer basket (d) farberware cutting board (e) Plastic comb

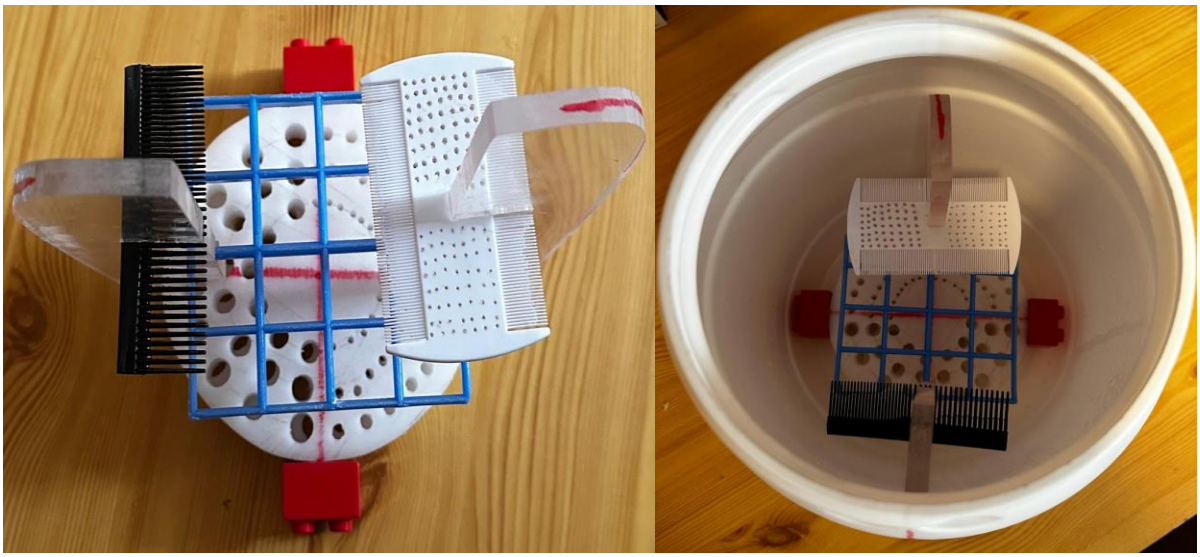

a b

Figure 3.1An image of a) the phantom insert b) the newly designed phantom

3.3 Measurement protocol.

Two sets of clinical MRI systems, Siemens - MAGNETOM Avanto fit and Siemens Biograph mMR were used to acquire the MR images during the QC process. The MAGNETOM Avanto fit is a 1.5 T field strength MR scanner that was used for the QC. The scanner has a bore size of 60cm with a system length of 160 cm. The strength of the gradient is 45mT/m at 200T/m/s and has zero helium consumption [30]. The Siemens biograph mMR, a 3 Tesla scanner in the PET/MRI center at St Olav Hospital was one of the main equipment which was also used for the scan. It is a hybrid system that integrates a positron emission tomographic system with magnetic resonance imaging in a single scanner [31]. It has a bore size and magnet length of 70 cm and 199 cm respectively. However, with the PET imaging embedded in the MRI system, the actual bore size for imaging is reduced to 60 cm. It is a zero-helium consumption with a gradient strength of 45mT/m at 200 T/m/s and an axial field of view of 258 mm [32]. During the image acquisition, a head coil with twenty channels was used. The new phantom was mounted on the table of the MRI scanner. The Phantom was positioned using the sagittal and axial lasers. It was also noted that the phantom was set such that its middle was located nearly or just in the middle of the head coil while aligning the isocenter of the scanner using the light indicators.

The phantom was then positioned so that the sagittal and axial lasers coincided with the axial and sagittal lines made on the surface of the phantom. A digital leveler was then used to confirm that the phantom was lying flat and symmetrical. To avoid discrepancies in measurements, the same procedure was repeated when setting up the ACR phantom for scanning. Figure 3.2 shows the setup of the phantom on the 3 T and 1.5 T respectively.

Figure 3.2 (a) Image of 3T Siemens Biograph mMR (b) Image of 1.5T Siemens - MAGNETOM Avanto fit, both with set up of the new phantom. The images were taken at St Olavs Hospital.

The first scan taken was the localizer image. A fast localizer image was acquired to be sure the phantom position was ok. If the image shows any misalignment of the phantom, we enter the room to set up the phantom again before any more scanning. A sagittal localizer image was then acquired for both the ACR and newly designed phantoms. A sagittal spin-echo acquisition through the phantom's middle serves as the localizer. T1-weighted imaging (T1WI) and T-2-weighted imaging (T2WI) were acquired using two axial spin-echo sequences in accordance with the ACR guidelines [20]. The scanning procedures for the ACR imaging followed a fixed set of protocols based on the ACR recommendations, whereas the scanning protocols were modified for the newly created phantom to accommodate its unique specifications and design. For example, due to the relatively longer length of the new phantom, it was important to increase the field of view as well as the number of slices to be able to cover the whole bottle. As a result of altering the scan protocols to fit the specifications and design of the newly fabricated phantom, the scan time was extended. After all the necessary image series such as ACR T1, ACR T2, Phantom T1, Phantom T2, and Proton Density were acquired, they were saved in uncompressed or lossless compressed DICOM format on a USB disc. These saved files were then uploaded onto the RadiAnt DICOM Viewer software for subsequent image analysis. The table below depicts a summary of the parameters of scan protocols for both the ACR and newly fabricated phantoms.

Table 3.0 Tabulated parameters of the scan protocol [20]

Study Design	ACR sagittal localizer	ACR axial T1	ACR axial T2	New Phantom localizer	New phantom axial T1	New phantom axial T2
Pulse sequence	Spin echo					
TR (ms)	200	500	2000	200	2000	3400

TE (ms)	20	20	80	20	20	80
FOV (cm)	250	250	250	250	250	250
Number of slices	1	11	11	1	40	80
Slice thickness (mm)	10	5	5	20	3	3
Slice gap, (mm)	n/a	5	5	n/a	6	6
Number of Averages	1	1	1	1	1	1
Matrix (Frequency)	256	256	256	256	256	256
Frequency (phase)	256	256	256	256	256	256
Scan time (min: sec)	0:26	2:16	8:56	0:26	5:20	11:37

3.4 Image Analysis

To visualize and analyze image data both quantitatively and qualitatively, a DICOM viewer with the required onscreen measurement tools was needed. The RadiAnt DICOM (version 2022.1.1 developed by Medixant) viewer software program was used. This DICOM viewer software can display studies that are obtained from various imaging modalities PET, CT, MRI, Digital radiography, Mammography and to mention a few [33]. The images were imported and displayed on a PC using the software, which could perform basic manipulation of image functions such as adjustment of the window and level, magnification, mean signal assessment within an area of interest, and length measurement tool. Geometric accuracy, high-contrast spatial resolution, slice thickness accuracy, slice position accuracy, image intensity uniformity, ghosting ratio, low-contrast object detectability, and artifact assessment were the image data that were evaluated. The figure below shows the interface of the software with loaded scans from the MR QC.

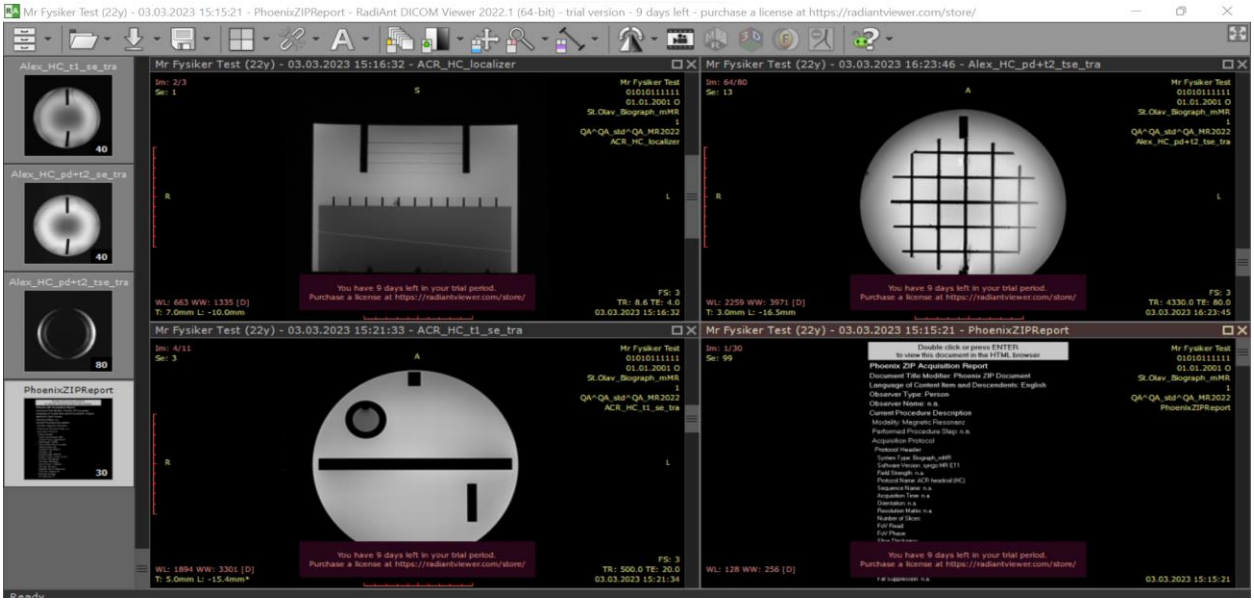

Figure (3.3) Screenshot of RadiAnt DICOM Viewer with DICOM images

3.4.1 Geometric accuracy analysis

The sagittal localizer image of the ACR phantom was shown. The window width and window level were adjusted so that the edges of the images are clearly seen. The upper to lower phantom lengths were measured along a line close to the phantom's center.
The T1 series of images were then displayed and the window and level were adjusted as shown in Figure 3.4. The axial diameters of the phantom in two directions from up to down and left to right were then measured.
Scrolling to the next slice with square grids, axial distances were measured in four different directions from top-to-bottom, left to right, and the diagonals. The same procedure was then repeated for the newly designed phantom.
The sagittal lengths of both phantoms were measured using the on-screen measurement tools of the software.
The measured values were compared to actual sagittal and axial phantom lengths and the deviations were then calculated and compared to tolerance levels [20]

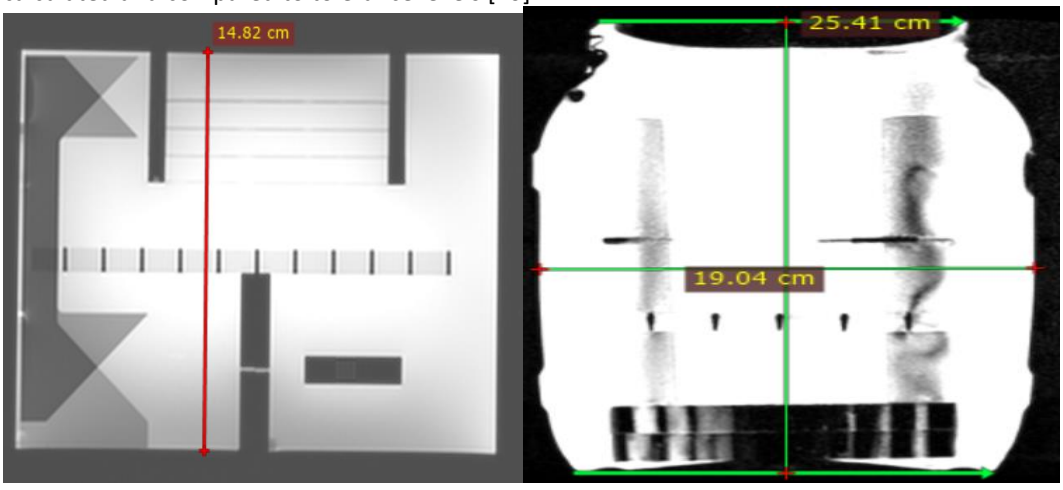

a b

Figure 3.4 Screenshot of an image localizer showing measurement from superior to inferior. a) ACR and b) New Phantom

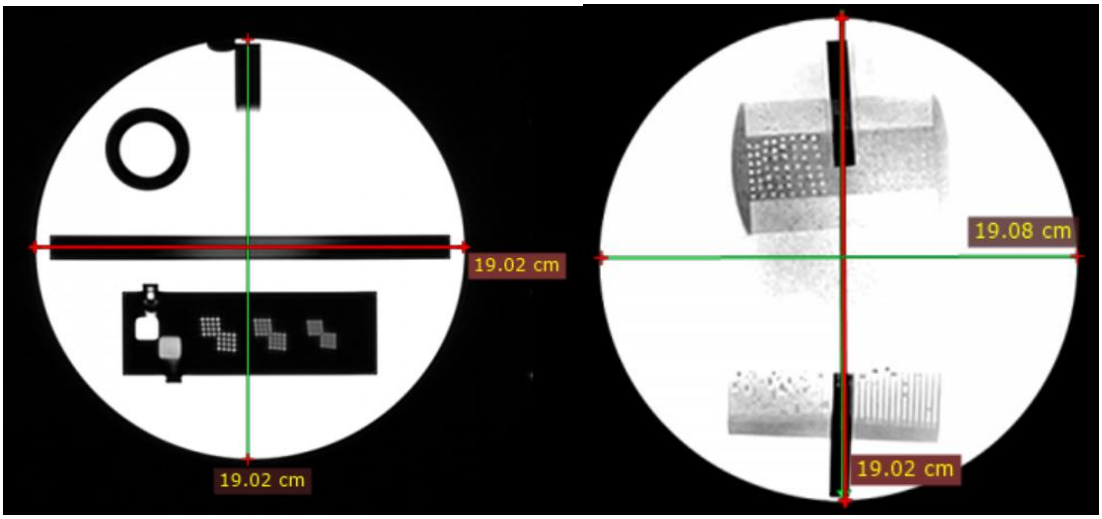

Figure 3.5 Axial slice showing the diameter measurements ACR (Left), New phantom (right).

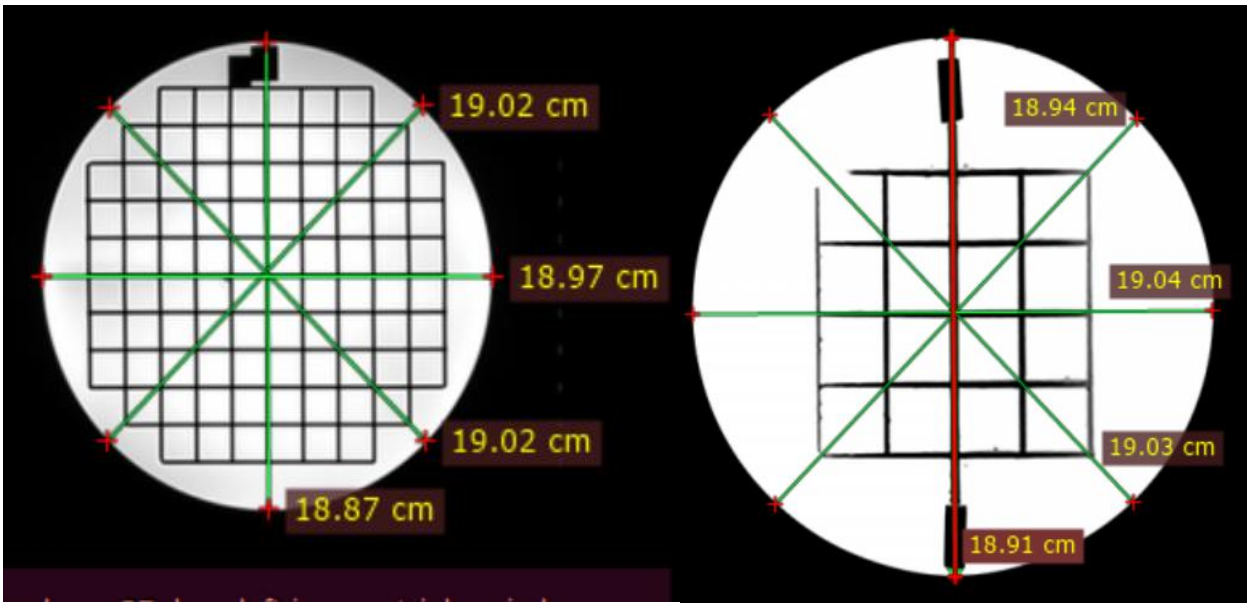

a b

Figure 3.6 Screenshot of the slice with grids of the (a) ACR and (b) New phantoms showing measurements of diameter in green lines

3.4.2 Assessment of high-contrast spatial resolution

Individual small bright spots in arrays of closely separated small holes were visually assessed for distinguishability of high-contrast spatial resolution. The bright spots which are observed are holes filled with water that were drilled into the plastic comb and it is called the resolution insert for the new phantom. To assess resolution the slices with resolution insert images for both phantoms were displayed. While the resolution insert was kept visible, the

images were magnified by some factor of two to four. The display window and the level were adjusted to clearly show that each hole could be distinguished from the other while keeping the array of holes checked. Beginning with the largest pair of holes, that is 1.1 mm hole diameter for both ACR T1 and ACR T2 image series, the holes were counted either by row or column. The image was then scored as resolved from right to left at the specific size of the hole provided all the four holes in any single row or column are distinguishable from one another for the ACR image series and the same for the fabricated phantom if all holes are clearly distinguished from each other. For ACR T1 and ACR T2 as well as the new phantom T1 and new phantom T2 image series, the inspected resolution in both directions were then recorded and the results were then compared with acceptance levels [20]. Additionally, the spatial resolution is assessed for the new phantom using the lines in the comb. If the 1.0 mm comb lines are clearly distinct from each other, then the image is said to have passed the test.

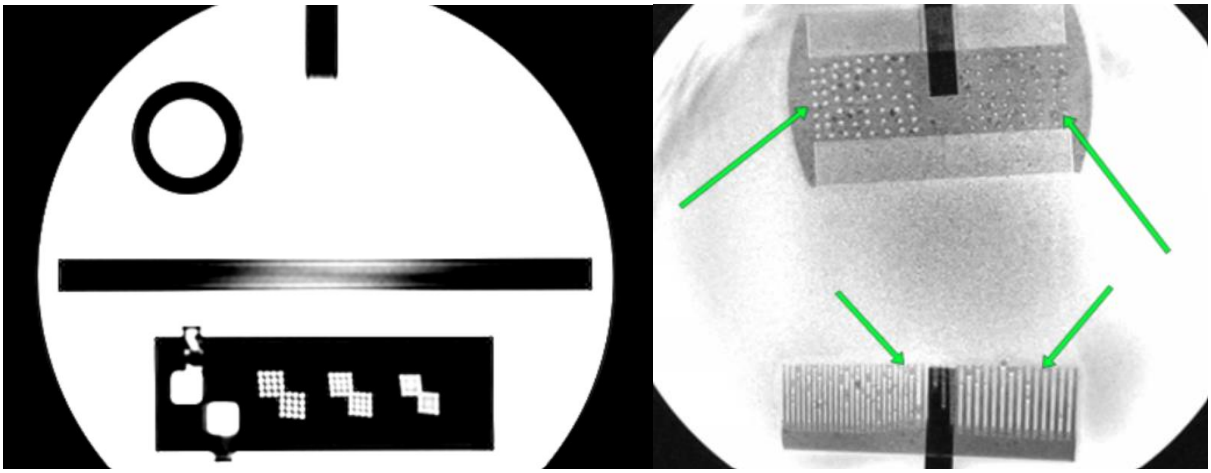

Figure 3.7 Portion resolution insert a slice of ACR (left) and new (right) phantoms illustrating visual assessment of high-contrast resolution on 3T scanner

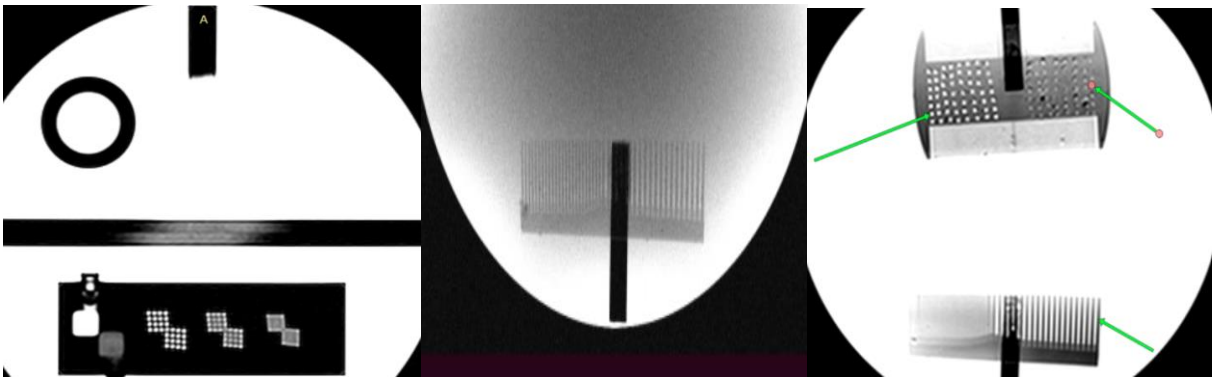

Figure 3.8 Portion resolution insert a slice of ACR (left) and new (middle and right) phantoms illustrating visual assessment of high-contrast resolution on 1.5 T scanner

3.4.3 Analysis of slice thickness accuracy.

To calculate the slice thickness, the top, and bottom signal ramp lengths were measured for all the axial series for the ACR phantom. To do these measurements, the slice with slice thickness insert was displayed and the image was then magnified to keep the insert clearly visible. To better visualize the signal ramps, the display level was adjusted. By placing an elliptical or rectangular ROI at the center of each ramp as shown in Figure 3.9, the mean signal values of both ROIs were noted. The average of the mean signal values was then calculated and the display level was then lowered by half the average ramp signal while setting the window to its minimum. The top and

bottom lengths of the ramps were then measured and recorded. The values for top and bottom ramp lengths were used to calculate the slice thickness using Equation 1 and the results were compared to the prescribed slice thickness. The deviations were then checked to see if they were within acceptable limits [20].

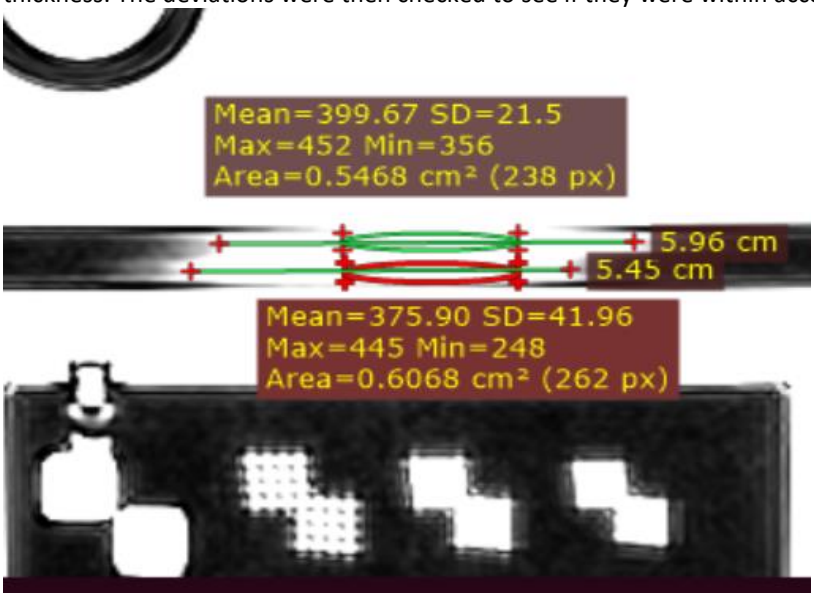

Figure 3.9 Screenshot of enlarged areas of slice displaying slice thickness signal ramp ACR

3.4.4 Image analysis for slice position accuracy

The variations between the prescribed and actual locations of slices 1 and 11 are determined for the ACR T1 and T2 series in this test. To measure this, an image in slice 1 was displayed and the size was magnified by some factor of say two to four. While magnifying the image, it was ensured that the vertical bars of the cross wedges were visible in the magnified portion of the image. For sharp and well-defined vertical bar ends, the display level was adjusted to be narrow while we measure and record the length difference between the left and the right bars. The measured bar length difference was then compared to the acceptable limit in [20].

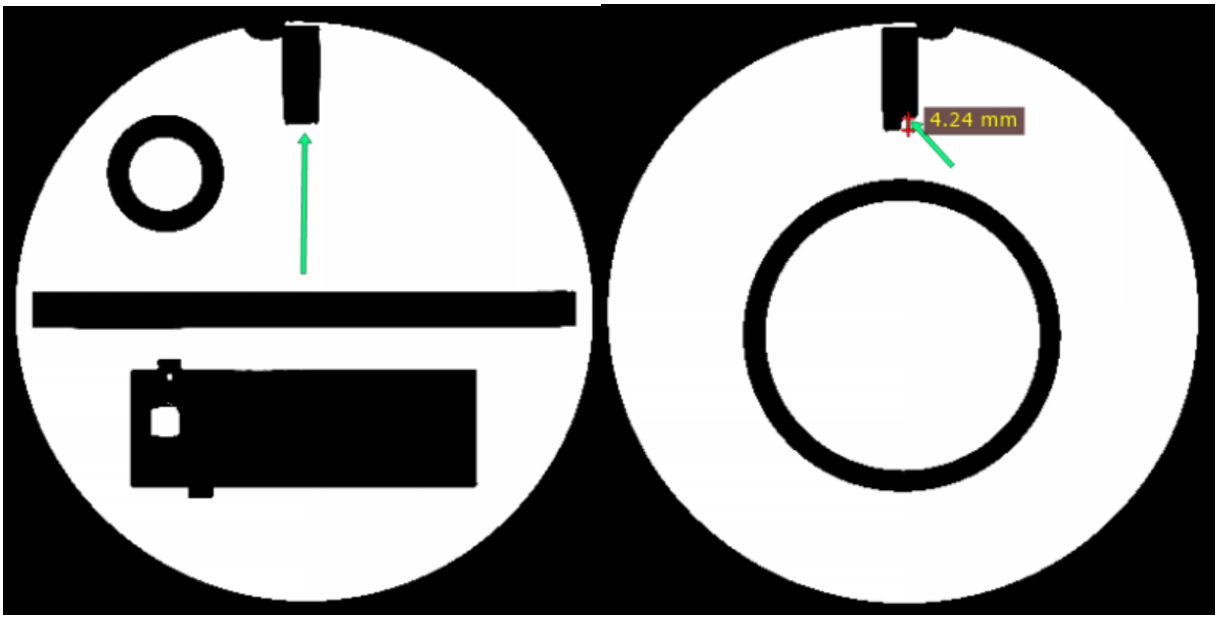

(a) (b)

Figure 3.10 Image of slice 1 showing measurements of error in slice position. a) Length difference between the right bar is small and typical of a well-positioned slice. b) The bar on the left of figure b is longer and the slice is inferiorly mispositioned.

3.4.5 Measurements of image intensity uniformity

The measurements for each series were taken using the following method:
The slice location with only water was shown and a large ROI was drawn on the displayed image as shown in Figure 3.11. The image uniformity measurements were performed on this large ROI. By making the whole area in the large ROI white, we reduced the window to the minimum while adjusting the level until the desired display was shown. Next, a $1cm^2$ circular round ROI was placed on the area of low signal, and the level was increased until it reached the desired level. The value for the mean signal intensity of the region of the low signal was then recorded. Furthermore, the display window and level were then set to default. The window and level were then again adjusted until the whole region in the large ROI was black with only a small portion showing some bright spots. This region of bright spots was the region of high signal intensity. A $1cm^2$ circular round ROI was then placed on this region and the mean signal intensity for the region of the high signal was also recorded. The percent image uniformity was calculated using high and low mean signal intensity values obtained and the results were compared to acceptable limits for both ACR and new phantom on a set of clinical MR systems.

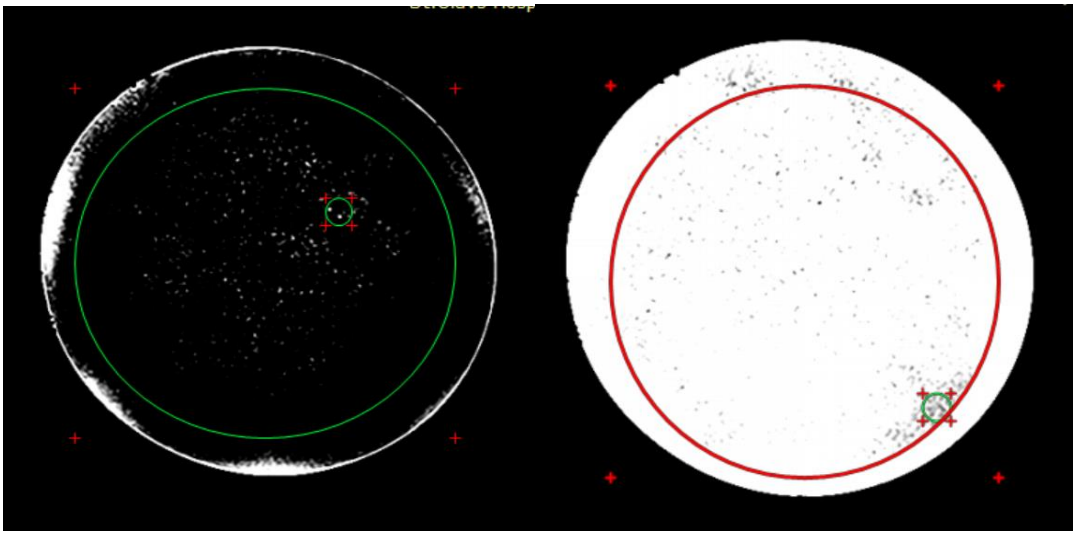

(a) (b)

Figure 3.11 Screenshot of a slice of the new phantom displaying windowed images with small ROI placements. (a) high signal evaluation and (b) low signal evaluation

3.4.6 Ghosting Analysis

The ghosting test was done by displaying image series T1 for both ACR and new phantoms. First, a large round ROI was drawn on the displayed slices shown in Figure 3.12 using the onscreen measurement tools. The mean pixel value for this ROI was noted and recorded. Using the onscreen tools again, elliptical ROIs of size about 10 cm^2 were drawn within the background. This is illustrated in Figure 3.13. By taking note of which ROI has which value, all the ROIs mean pixel values were recorded for the top, bottom, left, and right elliptical ROIs. The mean pixel values for the large ROI and the four small ROIs were used to calculate the ghosting ratio using Equation 3 The results were then compared to the tolerance level for the ghosting ratio.
The figure below shows an illustration of how measurements were done for large ROI and small ROIs with a blue arrow pointing to large ROI and a green arrow pointing to small ROIs in the background.

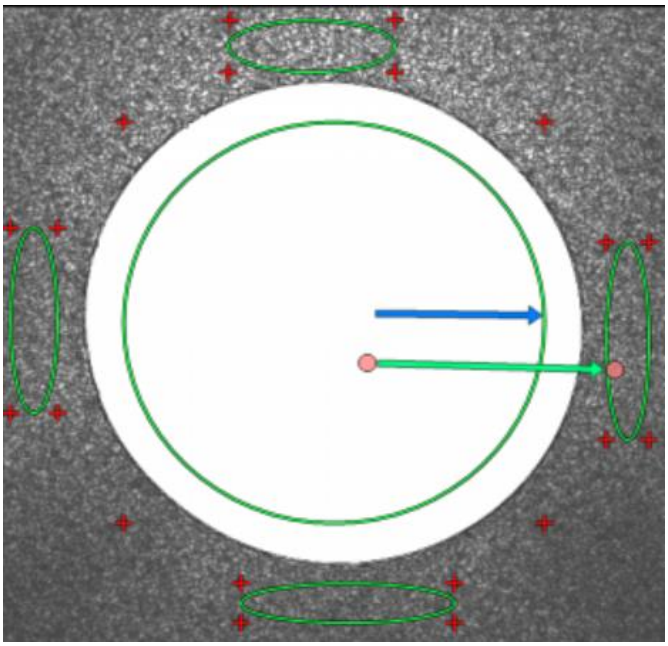

Figure 3.12 Screenshot of an image displaying placement of large and small ROIs for ghosting calculations.

3.4.7 Image assessment for Low-contrast object detectability

To detect objects of low contrast, the total number of spokes that were discernible on all the round discs for both ACR T1 and ACR T2 as well as new phantom T1 and T2 image series were counted. For the ACR phantom, the LCD section on slice 11 was displayed. This slice contains the highest number of contrast objects. The display width together with the window level was then adjusted until the low-contrast objects were clearly visible. To do this, the window width was carefully lowered while adjusting the level to best differentiate objects. The total number of spokes was then counted starting from the spoke with the highest diameter. In a clockwise direction starting from the first spoke, the counting was done until it got to a spoke where one or more of the disks could not be distinguished from the background. The complete number of spokes was noted. The same steps were repeated for the rest of the LCD images. The total number of spokes for each LCD and the results were compared to the acceptance limits for low-contrast object tests.

a) Slice 11 b) Slice 10 c) Slice 9 d) Slice 8

Figure 3.13 images of slice 11 to slice 8 displaying holes of objects of low contrast for ACR phantom

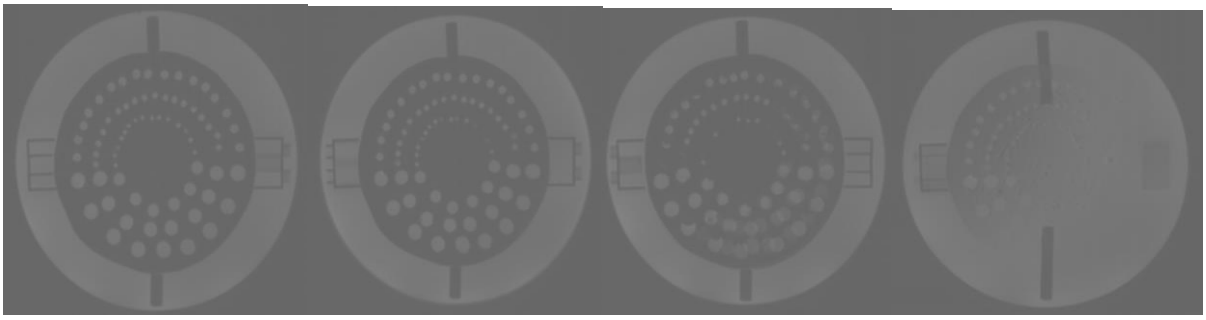

a) Slice 36 b) Slice 35 c) Slice 34 d) Slice 33

Figure 3.14 images of slice 36 to slice 33 displaying holes of objects of low contrast for new phantom

CHAPTER FOUR

4.0 RESULTS AND DISCUSSIONS

4.1 Results

Using the ACR phantom, all ACR MRI quality assurance tests were completed successfully using the routine clinical protocol for the ACR QC. Measurement protocols were designed for T1 and T2 phantom measurements for both 1.5T and 3T MRI scanners. The analysis of MRI images with RadiAnt Image viewer Software revealed that the image quality standards were within ACR regulations for the examined protocol.

4.1.1 Geometric accuracy

The sagittal lengths were found to be 148.7mm and 254.60mm for ACR and the new phantoms with axial diameters of 189.87mm and 190.06 mm respectively. These measurements for geometric accuracy were accepted with tolerance values according to ACR guidelines. Table 4.0 shows a summary of internal dimensions and geometric accuracy limits for ACR and the new phantoms.

Table 4.0 Table of results showing internal dimensions of both ACR and New Phantom with acceptable limits for GA.

Phantom	Sagittal length (mm)	Sagittal deviations (mm)	Axial diameter (mm)	Axial Deviations (mm)	Acceptance Limits (mm)
ACR large	148		190		
New Phantom	255		190		
ACR on1.5 T	148.70	0.70	189.83	0.17	± 2
ACR on 3 T	148.20	0.20	189.87	0.13	
New phantom on 1.5 T	254.60	0.4	190.76	0.76	
New phantom on 3 T	254.10	0.9	190.03	0.03	

4.1.2 High - Contrast Spatial resolution

The whole three pairs of arrays were visible on both ACR T1 and T2 slices as shown in figure 3.14.1, where they were seen at the lower side of the slices for both 3T and 1.5T scanners. As for the new phantom, both T1 and T2 slices showing the resolution inserts were clearly visible. Different hole diameters and line spacing were discernible by visually inspecting. The data in Table 4.1 depicts a summary of scoring for high contrast spatial resolution of the images on different sets of clinical MRI field strength.

Table 4.1 Table of results for ACR and New phantom resolution in pass/fail criteria

Field strength	Test	Object size (mm)	Pass/Fail (Rows)	Pass/Fail (Column)
3 T	ACR T1	1.0, 0.9, 0.8	Resolved	Resolved
	ACR T2	1.0, 0.9, 0.8	Resolved	Resolved
	NP T1	1.1, 1.0, 0.9, 0.8, 0.5	Resolved	Resolved
	NP T2	1.1, 1.0, 0.9, 0.8, 0.5	Resolved	Resolved
1.5 T	ACR T1	1.0, 0.9, 0.8	Resolved	Resolved
	ACR T2	1.0, 0.9, 0.8	Resolved	Resolved
	NP T1	1.1, 1.0, 0.9, 0.8, 0.5	Resolved	Resolved
	NP T2	1.1, 1.0, 0.9, 0.8, 0.5	Resolved	Resolved

NP= New Phantom

4.1.3 Slice Thickness Accuracy

The top and bottom ramps for both ACR T1 and ACR T2 were used to calculate the slice thickness and the results were compared to the actual slice thickness. The thickness of the slice for the phantom was also calculated and compared to the true thickness used for the imaging protocol. The results were then summarized in the table below.

Table 4.2 Top and bottom lengths for ACR and New phantom on field strengths 3T and 1.5T for slice thickness calculation

Field strength	Series	Top (mm)	Bottom (mm)	Measured Slice Thickness (mm)	True Slice thickness (mm)	Deviation (mm)	Tolerance level (mm)
1.5T	ACR T1	51.7	53.7	5.27	5	0.27	0.7

	ACR T2	52.3	53.4	5.28		0.28	

4.1.4 Slice Position accuracy

The slice position accuracy was evaluated on both 3T and 1.5T scanners. The bar length differences were measured for both ACR T1 and ACR T2 for the ACR phantom. These were then compared to the action criteria to determine if the scanner passes or fails this test. The results of bar length measurements and action criteria for a set of clinical MRI scanners are summarized in the table below.

4.3 Table of measured bar lengths with acceptance limits for slice position accuracy assessment.

Nominal Field Strength (T)	Protocol	Slice number	Measured bar length (mm)	Accepted bar length(mm) <=5mm	Pass/Fail criteria
3T	ACR T1	1	0	5	Pass
		11	4.24		Pass
	ACR T2	1	0		Pass
		11	4.61		Pass
1.5T	ACR T1	1	1.3		Pass
		11	3.0		Pass
	ACR T2	1	0.6		Pass
		11	2.65		Pass

4.1.5 Image intensity uniformity

The region of high and low signal values was measured for the ACR series and tabulated in Table 4.4. The results were used to calculate the percent image uniformity for both ACR and phantom respectively. Furthermore, the difference in percent image uniformity was observed for images taken right after setting up the phantom and thirty minutes afterward. Figure 4.2 and Figure 4.3 clearly show this by visual inspection. To quantify for results, the percent image uniformities were then calculated and compared to acceptable limits as shown in Table 4.4. Table 4.4 depicts measurements of high and low signal intensities and calculated PIU for both ACR and phantom.

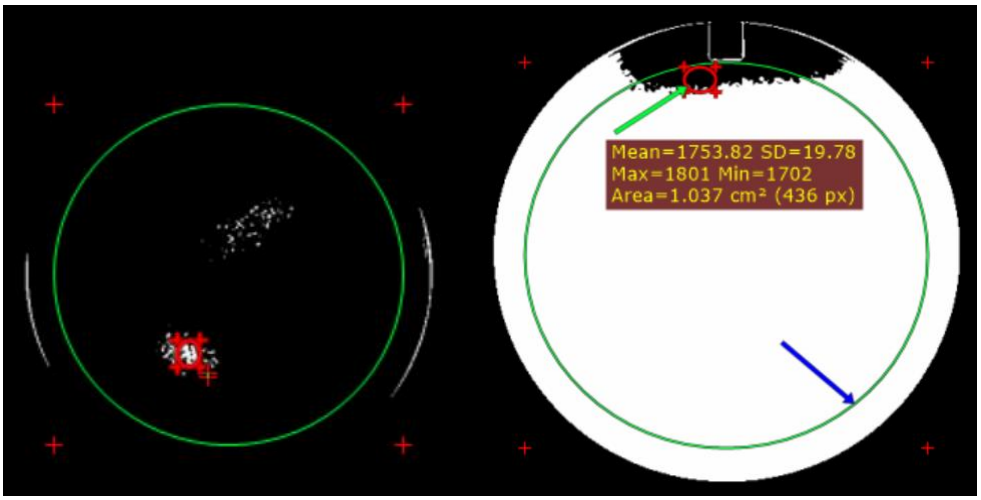

Figure 4.0 Screenshot of new phantom illustrating measurements of high(left) and low (right) intensities of new phantom (green and blue arrows showing small and large ROIs respectively)

on 1.5T

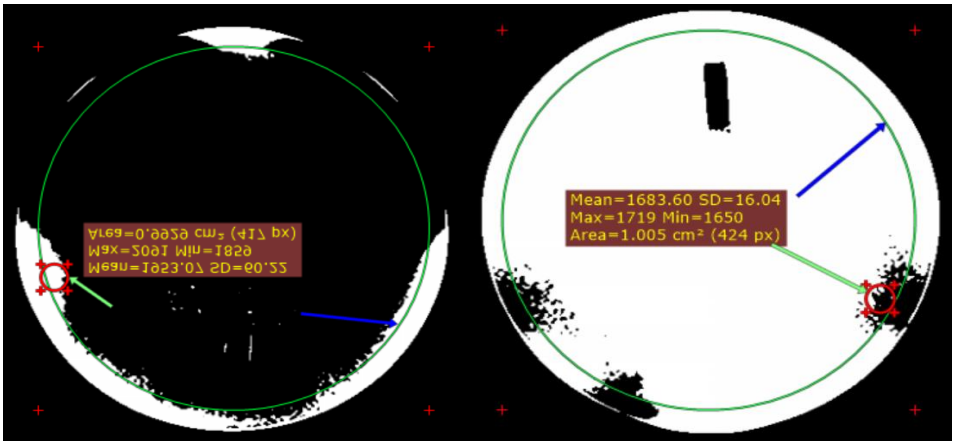

Figure 4.1 Screenshot of new phantom illustrating measurements of high(left) and low (right) intensities of new phantom (green and blue arrows showing small and large ROIs respectively for 3T.

Table 4.4 ROI sizes for PIU of ACR and New phantom calculations with acceptance criteria by field strength

PIU	Mean intensity High	Mean intensity low	PIU (%)	field strength	Pass/Fail Limit (%) = 3T
ACR T1	2656.84	2008.95	86.11	3T	>80
ACR T2	2840.36	2154.87	86.28		
New Phantom T1	1104.38	754.56	81.18		
New Phantom T2	1581.09	1249.05	88.26		
ACR T1	2012.68	1753.82	93.13	1.5T	≥85
ACR T2	2085	1829.36	93.47		
New Phantom T1	528.79	472.90	94.42		
New Phantom T2	1953.07	1683.60	92.59		

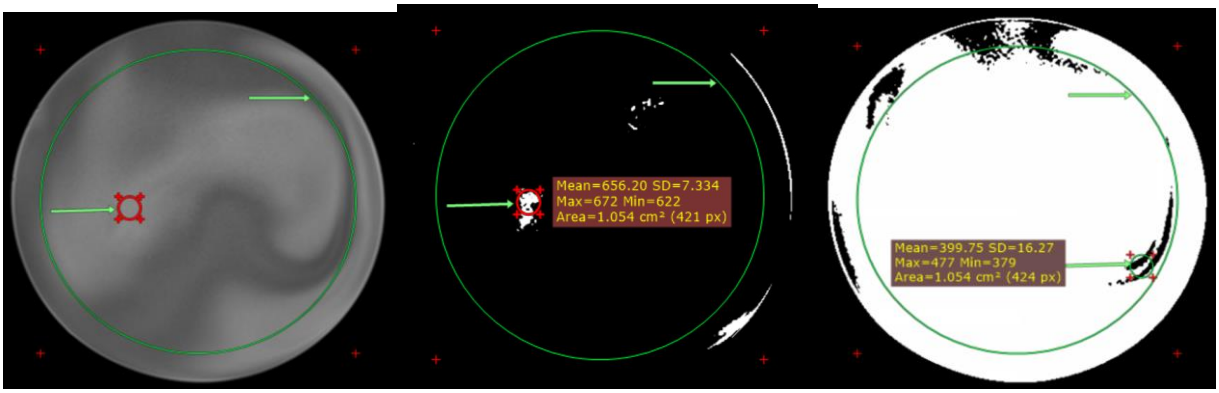

(a) (b) c)

Figure 4.2 Screenshot of slice showing a non-uniform image of the new phantom which was taken just after the phantom was set up (a) default image without windowing (b) Windowed image to show region of high intensity (c)Windowed image to show the region of low-intensity

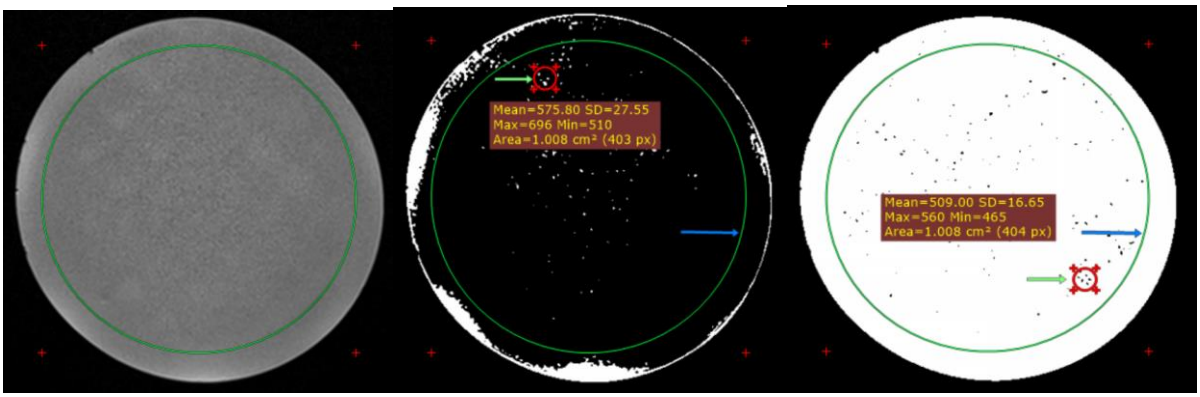

(a) (b) (c)

Figure 4.3 Screenshot of slice showing a non-uniform image of the new phantom which was taken 30 minutes after the phantom was set up (a) default image without windowing (b) Windowed image to show the region of high intensity (c) Windowed image to show the region of low-intensity

Table 4.5 ROI sizes for PIU of fabricated phantom measurement for two different waiting times.

PIU	Mean intensity High	Mean intensity low	PIU (%)	field strength	Acceptance limit for 1.5T(%)
New Phantom T1 before 30 mins	656.20	399.75	75.71	1.5T	87.5
New Phantom T1 after 30 mins of waiting time.	575.80	509.00	93.84	1.5T	

4.1.6 Ghosting

The ghosting ratio was computed from the seventh slice of the ACR series. The mean signal intensities of the large ROI, top, bottom, left, and right were measured as shown in Figure 4.4 and results were then tabulated as shown in Table 4.6 below.

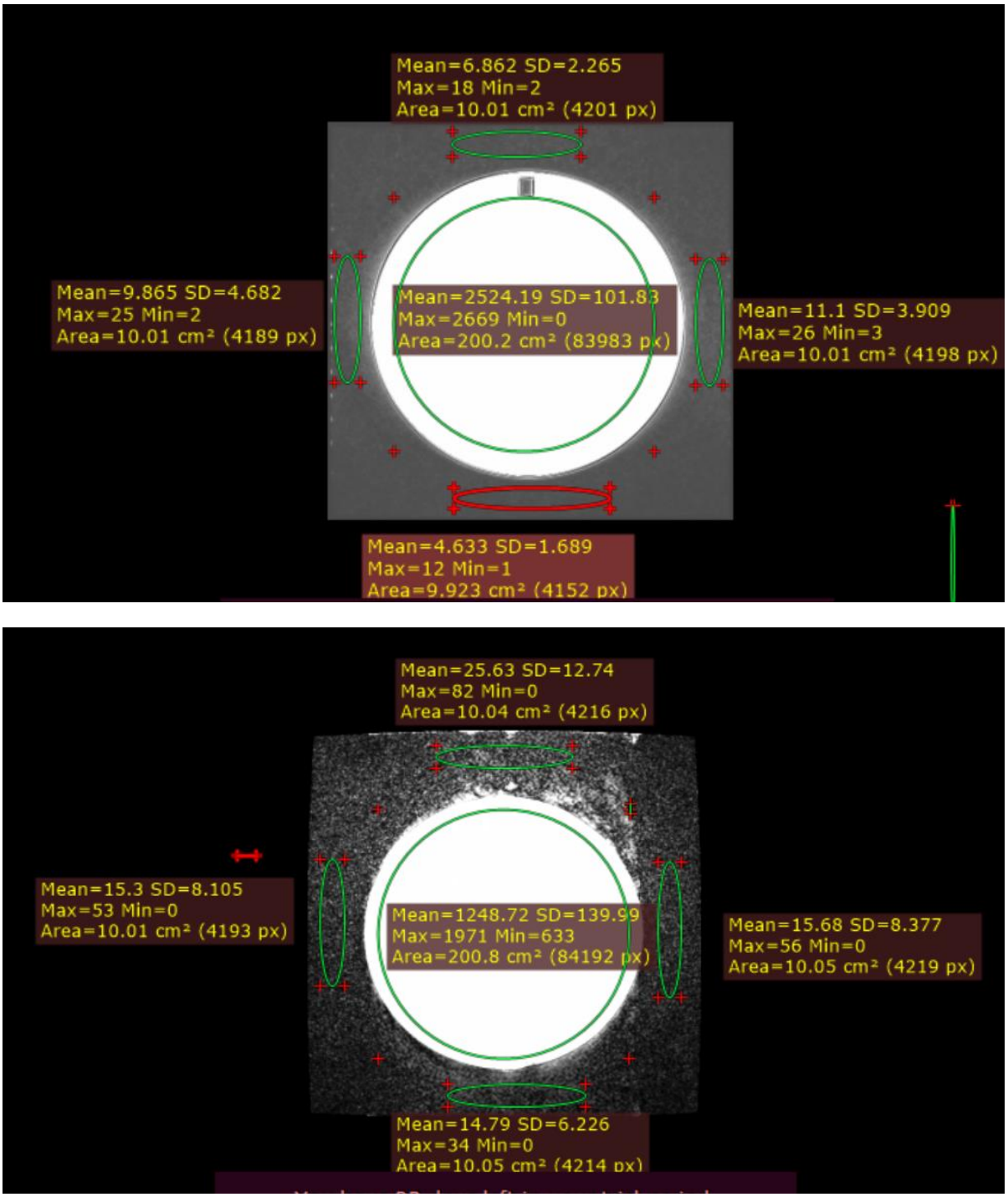

Figure 4.4 Screenshot of an image illustrating ROI placement for the percent signal ghosting

Table 4.6 ROI Pixel values for ACR and fabricated phantom measurements. Percent signal ghosting acceptable limits

Phantom	Mean pixel value (large ROI) px	Mean pixel value (Top)px	Mean pixel value (Bottom)px	Mean pixel value (Left)px	Mean pixel value (Right)px	Ghosting ratio	Percent signal ghosting (%)	Acceptable limit %
ACR T1 (3.0T)	83983	4201	4142	4189	4198	22/83983	0.026	</=3
ACR T1 (1.5T)	83895	4193	4174	4217	4219	23/55930	0.04	
New Phantom T1 (3.0T)	84192	42176	4214	4193	4219	19/168384	0.011	
New Phantom T1 (1.5T)	80036	3996	4003	4012	4012	25/160072	0.016	

4.1.7 Low-contrast object

The disks for low-contrast object detectability were observed from the eleventh slice through the eighth slice. The total number of spokes counted for both the ACR T1 and ACR T2 series as well as the new phantom on a set of clinical MRI scanners were noted. Table 4.7 shows the sum of spokes with acceptable limits for both the ACR T1 and ACR T2 image series.

Table 4.7 Total number of spokes counted for ACR and New Phantoms for LCD tests with acceptable limits

Nominal field strength	ACR T1 LCD Limit (total spokes)	ACR T2 LCD Limit (total spokes)	ACR T1 LCD measured (total spokes)	ACR T2 LCD measured (total spokes)	New Phantom T1 LCD Measured (total spokes)	New Phantom T2 LCD Measured (total spokes)	Actual number of spoke for new phantom
1.5T	≥30	≥25	36	31	279	276	300
3T	≥37	≥37	38	38	286	292	

4.2 Discussion.

The newly designed phantom together with the ACR phantom has been used for several studies and standard QCs which include but are not limited to geometric accuracy, high contrast spatial resolution, slice position accuracy, slice thickness accuracy, image intensity uniformity, ghosting ratio, and low contrast object detectability. The intent of designing the new phantom was basically to be used for these standard measurements proposed by the ACR in MRI quality assurances and tests for MRI QA.

Using the ACR T1 imaging protocol for quality assurance on MRI scanners, the first image sequence on the new phantom was taken. During the first image sequence, a sagittal localizer slice was taken, and several artifacts were observed in the images as depicted in Figure 4.2. These artifacts were attributed to the movement of water molecules in the phantom. To mitigate these artifacts, the phantom was allowed to settle for about 30 minutes to reduce flow-induced artifacts. Another scan was then performed, and clear images with minimal artifacts were obtained as observed in Figure 4.3. It is noteworthy that even slight vibrations in the water during table movement can result in motion artifacts. Therefore, it is highly recommended to allow the new phantom to settle for 30 minutes after setup before scanning, unlike the ACR phantom, to improve image quality by minimizing motion artifacts. The ACR phantom does not have motion artifacts in the images because of the specific properties of its gelatin-based solution. This solution is designed to minimize any flow or movement during imaging and provide a stable matrix for test objects. The consistent magnetic susceptibility of the solution also helps to decrease susceptibility artifacts in the images. Furthermore, prior to filling the phantom, the solution is degassed to prevent bubbles or other artifacts. The combination of these factors ensures that the ACR phantom produces images without motion artifacts [34, 35, 36].

In terms of geometric accuracy testing, the evaluation of sagittal length and axial diameter indicated that both scanners met the tolerance values established by the ACR guidelines, with maximum deviations of 0.17mm and 0.76mm for the ACR phantom and the new phantom, respectively. These values fell within the acceptable tolerance range of ±3 mm set forth by the ACR guidelines. The new phantom was found to be particularly well-suited for geometric accuracy measurements, with the square grid insert providing effective guidance for the measurements.

In the evaluation of the new phantom's high-contrast spatial resolution test, a specific FOV and matrix were chosen for the axial series to produce pixel sizes of 1.0 mm in both directions. Upon visual inspection, it was observed that both the ACR and new phantom could distinguish holes with a diameter of 1.0 mm. The further assessment demonstrated that the new phantom could also distinguish 0.9 mm line spacing and discernible comb line spacing of 0.5 mm, as depicted in Figure 3.8. The resultant images from the new phantom were scored as resolved, indicating the effective performance of the new phantom in the high-contrast object detectability test. Notably, both scanners passed ACR T1 and ACR T2 for both phantoms, as illustrated in Figures 3.7 and 3.8. The new phantom's ability to resolve objects as small as 0.5 mm in size underscores its potential as an alternative for MRI high contrast spatial resolution test phantom.

The measured slice thickness for both the ACR T1 and T2 series should be 5.0mm ± 0.7mm for the ACR phantom measurements [20]. Analysis of slice thickness accuracy showed that the measured slice thickness for the ACR phantom on both 3T and 1.5T clinical MRI systems were within acceptable limits. It was not possible to evaluate the accuracy of slice thickness for the new phantom because there was no equipment available to create ramps required for the thickness measurements. This is a drawback of the new phantom that needs to be addressed in a future updated version by finding an alternative solution

For the slice position accuracy test the lengths of the two special bars in slices 1 and 11 in the ACR phantom were measured for both ACR T1 and T2 series. Analysis of bar lengths showed that all measurements were within the accepted limits of 5mm [20] as shown in (Table 4.3). However, measurements of slice position could not be done for the newly developed since the cross wedges needed special crafting and technique and there was not much time for it. Another reason could also be that the idea of the project is to design a phantom at a very low cost and involving skilled and technical designs would have increased the cost. Nevertheless, future development could add

slice position inserts for slice position measurements. One suggestion could be exploring the impact of 3D printing on this crafting.

The accuracy of slice thickness can be impacted by a number of factors, including inaccurate slice prescription, table positioning errors, poor gradient calibration, and B0 homogeneity issues. These individual factors may be severe enough to cause a failure in slice position measurements for the ACR phantom, but may not be observed in the new phantom [37-41]. Additionally, nonlinearity in the radiofrequency (RF) amplifier can cause distorted RF pulse shapes, potentially leading to failure in the slice thickness accuracy test. Similarly, miscalibration or poor gradient calibration, or switching performance can also lead to test failure. If both slice thickness accuracy and slice position accuracy fail, it can negatively impact the low-contrast object detectability test [37-41].

For the image intensity uniformity test, the PIU was calculated to be 86.11% and 86.28% for the ACR phantom, T1, and T2 series respectively on the 3T MRI system. PIU for the new phantom was also computed to be 81.18 and 88.26% on the 3T system. In each case of the two phantoms, the calculated PIU was greater than or equal to 80% which was in perfect agreement with the acceptance criteria of 80% for 3T field strength systems [20]. Further analysis showed that PIU values of 93.13%, 93.47%, 94.42%, and 92.59% were calculated for ACR T1, ACR T2, new phantom, T1, and new phantom T2 respectively on the 1.5T field strength. Comparing these values with the tolerance levels for 1.5T, these values were greater than or equal to the 87.5% limits [12]. The new phantom showed excellent results to be used as an alternative phantom for QCs of image intensity uniformity test. Comparing values of PIU for images acquired on 3T and 1.5 T revealed that, PIU on 1.5T were greater than those found for the on the 3T. This could be accounted for by the increase in field inhomogeneities with increasing field strength. Higher field strength can pose challenges in achieving a perfectly homogeneous magnetic field, leading to image intensity variations and reduced image uniformity.

In order to quantify the impact of artifacts on an MRI image, the percent image uniformity (PIU) was calculated for an image taken immediately after setting up a new phantom, which resulted in a PIU of 75.71%. According to ACR guidelines [20], this value was outside the acceptable range for PIU. However, when the phantom was left to settle for 30 minutes, the calculated PIU increased to 93.84%, which was within the ACR tolerance level of 87.5%. These findings suggest that the new phantom is suitable for PIU measurements as long as it is allowed to settle for approximately 30 minutes prior to imaging.

The suitability of a new phantom for ghosting ratio testing was evaluated by comparing the results obtained from the new phantom to those obtained using the ACR phantom. The ghosting ratios for 1.5T and 3T systems were calculated for both phantoms using ACR T1 slice seven. The results showed that the ghosting ratios obtained from the new phantom were comparable to those obtained from the ACR phantom, with values of 0.00011 and 0.000156 for 3T and 1.5T systems, respectively. The corresponding percent ghosting values for the new phantom were 0.011% and 0.0156%, which were below the acceptable limits of 3%. Based on these findings, it can be concluded that the new phantom is suitable for ghosting ratio testing and can be used as an alternative to the ACR phantom. The low ghosting ratios and percent ghosting values obtained from the new phantom suggest that it can provide accurate and reliable measurements for this test. Therefore, the new phantom can be considered a valuable addition to quality control procedures for MRI systems.

For the low-contrast detectability the total sum of spokes 36 and 31 on the ACR T1 and T2 image series for the 1.5T system. The number of spokes counted on the 3T scanner was 38 for both ACR T1 and T2 series. Comparing this to the acceptable limits for ACR T1 and T2 series showed that low-contrast objects were clearly distinguishable as depicted by Table 4.7. The sum of spokes for the new phantom T1 and T2 series were found to be 286 and 292 on the 3T clinical MRI system. For the 1.5T system, the number of spokes was found to be 279 and 276 for phantom T1 and T2 series respectively. Based on the results obtained from the new phantom, it can be concluded that the low contrast detectability of the phantom was within acceptable limits. The total sum of spokes for the T1 and T2 series on both 1.5T and 3T systems was found to be comparable to the acceptable limits set by ACR. This indicates that low-contrast objects can be clearly distinguished from one another on both clinical MRI systems.

Furthermore, the low contrast detectability results obtained from the new phantom were found to be comparable to those obtained from the ACR phantom specifically for slices 11, 10, and 9 of the ACR series versus slices 36, 35, and 34 as shown in Figure 3.13 and Figure 3.14 respectively. This indicates that the new phantom is suitable for testing the low-contrast detectability of clinical MRI systems.

It is important to note that low contrast detectability is a critical parameter for assessing the image quality of MRI systems. The ability to distinguish low-contrast objects is essential for accurate diagnosis and treatment planning. The fact that the new phantom has shown to be suitable for this test indicates that it can be a valuable tool for quality control testing of clinical MRI systems.

From the quality assurance and quality control tests done using the fabricated phantom, it has been discovered that there are several limitations, however, with some potential improvements for the future development of the phantom. One specific challenge is that the slice position accuracy could not be analyzed using the newly fabricated phantom. Another limitation was that there was much waiting time for the solution in Phantom to settle to reduce artifacts due to flow. Last but not least, exact T1 and T2 values could not be achieved since the phantom was filled with just water containing 75mM salt solution. However, measuring T1 and T2 values is important for MRI quality control as it provides information about tissue characteristics, which can be useful in diagnosing various medical conditions. For instance, T1 values can be used to distinguish between different types of tissues, while T2 values can be used to identify areas of inflammation or edema. However, it is not possible to accurately measure T1 and T2 values in water containing only salt because salt has a negligible effect on these values. T1 and T2 values are primarily influenced by the type of tissue and the presence of other substances, such as fat or protein [42-46]. Thus, it is necessary to use phantoms that mimic the tissue characteristics of interest to accurately measure T1 and T2 values. These phantoms can contain materials such as agar, oil, or other substances that simulate the magnetic properties of various tissues [42-46]

During the time since the phantom was fabricated, there were not enough evidential articles on how to achieve T1 and T2 values using a simple recipe with widely available materials. Research done by Rios NL et al. revealed that one can achieve the desired T1 and T2 values such as the ACR phantom by obtaining a mixture that mimicked the average human tissue in the region of interest in terms of dielectric parameters and relaxation times. To do this, one had to find a trade-off between sugar and agar concentrations since both affect relaxation times, and sugar is used to control permittivity. This allowed it to keep the permittivity and relaxation times within the range of human tissues while still producing a gel. According to Rios NL et.al, by combining ingredients of Water (demineralized): 9,900 mL, Mouthwash (no alcohol): 600 mL (4% of final volume), Salt: 254 g, Sugar: 7,913 g, Agar: 116g (0.75% of final volume), one can make sucrose like a mixture for the phantom solution [47]. The amount of these ingredients could however change depending on the volume of solution one is making. A full description of a recipe on how to make the solution can be found in the article [47]. However, this article was not recovered until the phantom had already been designed. In view of this, it is recommended that future upgrades of this phantom should include a sucrose-based solution since this has the potential to achieve desired T1 and T2 values, reduce air bubbles in the solution and also reduce artifacts due to the motion of the liquid. Furthermore, future development of the phantom should also include adjacent wedges at 45 degrees to help ease measurements with respect to slice position.

CHAPTER FIVE (5)

5.0 Conclusions

A low-cost, easy-to-manufactured, and highly efficient alternative phantom with accompanying measurement protocols was successfully proposed and fabricated. The phantom as it stands could perform qc measurements on geometric accuracy, high-contrast spatial resolution, image intensity uniformity, Signal ghosting, and low-contrast object detectability test. The MRI scanner was tested with clinical scan protocols stated by the ACR MRI accreditation program for the ACR phantom while the scan parameters were altered for example the number of slices and the slice thickness which caused a change in echo and repetition time just to be able to cover all slices of the whole new phantom. For both scanners, all the ACR MRI qc tests were conducted successfully using the ACR and newly designed phantom with the exception of slice position accuracy for the newly designed phantom.
By implementing and comparing the results acquired with the new phantom to an existing (ACR) phantom on a set of clinical MRI systems (3T and 1.5T), the new phantom showed agreeable results which were discussed in Chapter 4. While the present design of the MRI system phantom could be upgraded and is not adequate for all calibration needs and QC, this is a very good effort at constructing a cost-effective, easy-to-use backup phantom with widely available materials that can be used for very successful QC on MRI scanners. In addition to this, the new phantom could be a valuable addition for system performance tests in regions like Africa where ACR phantoms are not widely available.

REFERENCES

[1] V. Kuperman, *Magnetic resonance imaging: physical principles and applications*. Elsevier, 2000.

[2] B. J. Hillman, E. S. Amis Jr, and H. L. Neiman, "The future quality and safety of medical imaging: proceedings of the third annual ACR FORUM," *Journal of the American College of Radiology,* vol. 1, no. 1, pp. 33-39, 2004.

[3] C. S. Lee, V. Wadhwa, J. B. Kruskal, and D. B. Larson, "Conducting a successful practice quality improvement project for American Board of Radiology certification," *Radiographics,* vol. 35, no. 6, pp. 1643-1651, 2015.

[4] A. C. o. Radiology, "Magnetic resonance imaging quality control manual," *Reston, VA: American College of Radiology,* 2015.

[5] G. Sreedher *et al.*, "Magnetic resonance imaging quality control, quality assurance and quality improvement," *Pediatric Radiology,* vol. 51, no. 5, pp. 698-708, 2021.

[6] C.-C. Chen, Y.-L. Wan, Y.-Y. Wai, and H.-L. Liu, "Quality assurance of clinical MRI scanners using ACR MRI phantom: preliminary results," *Journal of digital imaging,* vol. 17, no. 4, pp. 279-284, 2004.

[7] L. Mascaro, S. Strocchi, P. Colombo, M. Del Corona, and A. M. Baldassarri, "[Definition criteria for a magnetic resonance quality assurance program: multicenter study]," (in ita), *Radiol Med,* vol. 97, no. 5, pp. 389-97, May 1999. Criteri per la definizione di un programma per l'assicurazione della qualità nella diagnostica per immagini con risonanza magnetica: studio multicentrico.

[8] P. Bourel, D. Gibon, E. Coste, V. Daanen, and J. Rousseau, "Automatic quality assessment protocol for MRI equipment," *Medical Physics,* vol. 26, no. 12, pp. 2693-2700, 1999.

[9] T. W. Redpath and C. J. Wiggins, "Estimating achievable signal-to-noise ratios of MRI transmit-receive coils from radiofrequency power measurements: applications in quality control," *Physics in Medicine & Biology,* vol. 45, no. 1, p. 217, 2000.

[10] M. Firbank, R. Harrison, E. Williams, and A. Coulthard, "Quality assurance for MRI: practical experience," *The British Journal of Radiology,* vol. 73, no. 868, pp. 376-383, 2000.

[11] https://www.phantomlab.com/magphan-adni

[12] MRI in Practice, Fourth Edition. Catherine Westbrook, Carolyn Kaut Roth, John Talbot. page 307
© 2011 Blackwell Publishing Ltd. Published 2011 by Blackwell Publishing Ltd.

[13] B. Gruber, M. Froeling, T. Leiner, and D. W. Klomp, "RF coils: A practical guide for nonphysicists," *Journal of magnetic resonance imaging,* vol. 48, no. 3, pp. 590-604, 2018.

[14] Ballinger J, Murphy A, Bell D, et al. Magnets (types). Reference article, Radiopaedia.org (Accessed on 24 Apr 2023) https://doi.org/10.53347/rID-22573

[15] BlueShield Magnet. Koninklijke Philips N.V, 2018. (sales brochure)Superconduction.org website

[16] Hidalgo-Tabon SS. Theory of gradient coil design methods for magnetic resonance imaging. Concepts Mag Res Part A 2001; 36A:223-242. Lauterbur PC. Image formation by induced local interactions: examples employing nuclear magnetic resonance (pdf). Nature 1973; 242:190-191

[17] C. E. Hayes, W. A. Edelstein, J. F. Schenck, O. M. Mueller, and M. Eash, "An efficient, highly homogeneous radiofrequency coil for whole-body NMR imaging at 1.5 T," *Journal of Magnetic Resonance (1969),* vol. 63, no. 3, pp. 622-628, 1985.

[18] N. I. Avdievich, "Transverse Electromagnetic (TEM) Surface Coils for Extremities," *eMagRes,* 2007.

[19] M. Silver, R. Joseph, and D. Hoult, "Selective spin inversion in nuclear magnetic resonance and coherent optics through an exact solution of the Bloch-Riccati equation," *Physical Review A,* vol. 31, no. 4, p. 2753, 1985.

[20] ACR. *Phantom Test Guidance for the ACR MRI Accreditation Program.* American College of Radiology; Reston, VA: 2005.
[21] https://www.newmaticmedical.com/product/ACR-MRI-Phantom-ACRMRP
[22] https://www.medicaldevicedepot.com/Pro-Project-Pro-MRI-Phantom-p/09-101.htm
[23] https://www.standardimaging.com/products/pro-mri-phantom-kit
[24] Stupic, KF, Ainslie, M, Boss, MA, et al. A standard system phantom for magnetic resonance imaging. *Magn Reson Med*. 2021; 86: 1194– 1211. https://doi.org/10.1002/mrm.28779
[25] https://www.curtec.com/en/products/drums/wide-neck-drums/detail/wide-neck-drum-6-liter
[26]https://www.amazon.com/Farberware-Nonslip-Plastic-11-Inch-14-Inch/dp/B000W4OC80?th=1
[27] https://www.caterbox.co.uk/dishwasher-rack-range/glasswasher-baskets-500mm
[28] https://www.britannica.com/topic/LEGO
[29] https://www.lego.com/ms-my/sustainability/product-safety/materials/
[30]https://www.siemens-healthineers.com/en-us/magnetic-resonance-imaging/0-35-to-1-5t-mri-scanner/magnetom-avanto
[31]https://www.med.unc.edu/bric/human-imaging/human-imaging-modalities/pet-mr/#:~:text=The%20Siemens%20Biograph%20mMR%20represents,PET%20images%20in%20human%20subjects
[32]https://www.siemens-healthineers.com/en-us/magnetic-resonance-imaging/mr-pet-scanner/biograph-mmr
[33] https://www.radiantviewer.com/dicom-viewer-manual/index.htmlMedixant. RadiAnt DICOM Viewer [Software]. Version 2021.1. Aug 17, 2022. URL: https://www.radiantviewer.com
[34] J.W. Schulte et al. "ACR MRI phantom: design and implementation." Journal of Magnetic Resonance Imaging, vol. 2, no. 5, 1992, pp. 583-588.
[35] K.S. Kim et al. "ACR MRI phantom: magnetic susceptibility and T1 evaluation." Journal of Magnetic Resonance Imaging, vol. 4, no. 4, 1994, pp. 557-562.
[36] G.E. White et al. "ACR MRI accreditation phantom: a new system." Journal of Magnetic Resonance Imaging, vol. 15, no. 3, 2002, pp. 292-303.
[37] Webb, A. G. (2016). Introduction to biomedical imaging. John Wiley & Sons.
[38] Shung, K. K., Smith, M. B., & Tsui, B. M. W. (Eds.). (2011). Principles and technical aspects of MRI. World Scientific.
[39] American College of Radiology. (2015). ACR–AAPM–SIIM Technical Standard for Electronic Practice of Medical Imaging. American College of Radiology.
[40] Cramer, B. M. (2013). Quality assurance for diagnostic imaging equipment. Springer Science & Business Media.
[41] Kanal, E., Barkovich, A. J., Bell, C., Borgstede, J. P., Bradley, W. G. Jr, Froelich, J. W., ... & Zaremba, L. A. (2013). ACR guidance document on MR safe practices: updates and critical information 2013. Journal of magnetic resonance imaging, 37(3), 501-530.
[42] Busse, R. F., Brau, A. C., Vu, A., Michelich, C. R., Bayram, E., Kijowski, R., & Reeder, S. B. (2008). Effects of refocusing flip angle modulation and view ordering in 3D fast spin echo. Magnetic resonance in medicine, 60(3), 640-649. doi: 10.1002/mrm.21681
[43] Kecskemeti, S. R., & Sammons, G. S. (2018). Imaging Quality Control in the Era of Artificial Intelligence and Radiomics. Journal of Digital Imaging, 31(4), 393-398. doi: 10.1007/s10278-018-0079-4
[44] Madelin, G., & Regatte, R. R. (2015). Biomedical applications of sodium MRI in vivo. Journal of Magnetic Resonance, 253, 23-36. doi: 10.1016/j.jmr.2015.01.015

[45] Redpath, T. W., & Whittall, K. P. (1998). Measurement of T1 and T2 in the body: implications for MRI. Clinical Radiology, 53(8), 573-580. doi: 10.1016/S0009-9260(98)80041-8

[46] Smith, D. S. (2004). Introduction to magnetic resonance imaging techniques. Journal of Nuclear Cardiology, 11(5), 631-645. doi: 10.1016/j.nuclcard.2004.07.003

[47] Rios NL, Gilbert KM, Papp D, Cereza G, Foias A, Rangaprakash D, May MW, Guerin B, Wald LL, Keil B, Stockmann JP, Barry RL, Cohen-Adad J. 8-channel Tx dipole and 20-channel Rx loop coil array for MRI of the cervical spinal cord at 7 Tesla [Internet]. 2023. Available from: http://biorxiv.org/lookup/doi/10.1101/2023.02.08.527664

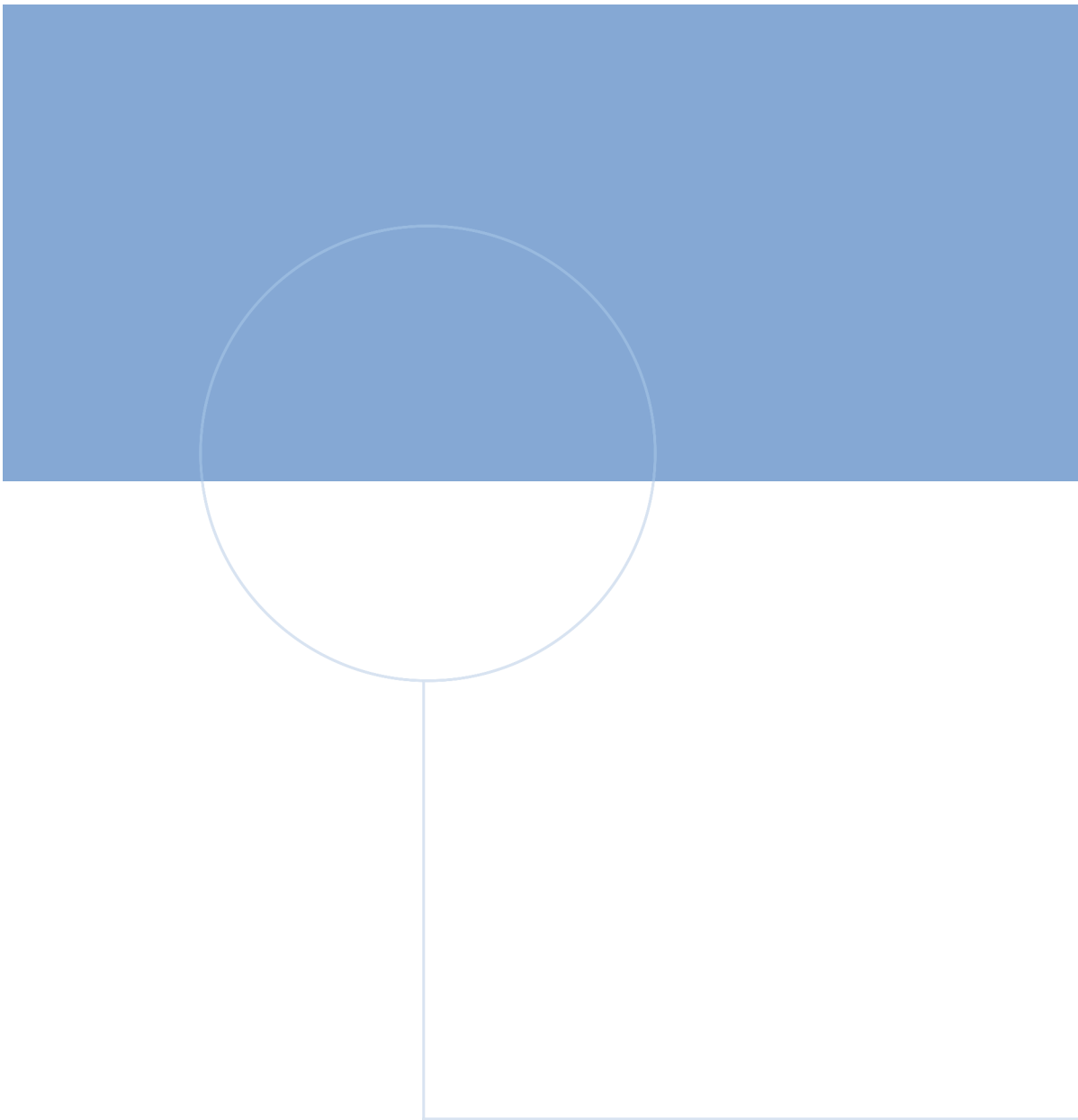

NTNU

Norwegian University of
Science and Technology